The Astronomical Journal, 160:235 (14pp), 2020 November https://doi.org/10.3847/1538-3881/abba3b


# TOI-481 b and TOI-892 b: Two Long-period Hot Jupiters from the Transiting Exoplanet Survey Satellite

Rafael Brahm[1,2], Louise D. Nielsen[3], Robert A. Wittenmyer[4], Songhu Wang[5], Joseph E. Rodriguez[6], Néstor Espinoza[7], Matías I. Jones[8,9], Andrés Jordán[1,2], Thomas Henning[10], Melissa Hobson[2,11], Diana Kossakowski[10], Felipe Rojas[2,11], Paula Sarkis[10], Martin Schlecker[10], Trifon Trifonov[10], Sahar Shahaf[12], George Ricker[13], Roland Vanderspek[13], David W. Latham[6], Sara Seager[13,14,15], Joshua N. Winn[16], Jon M. Jenkins[17], Brett C. Addison[18], Gáspár Á. Bakos[16], Waqas Bhatti[16], Daniel Bayliss[19], Perry Berlind[6], Allyson Bieryla[6], Francois Bouchy[3], Brendan P. Bowler[20], César Briceño[21], Timothy M. Brown[22,23], Edward M. Bryant[19,24], Douglas A. Caldwell[25,26], David Charbonneau[6], Karen A. Collins[6], Allen B. Davis[5], Gilbert A. Esquerdo[6], Benjamin J. Fulton[27], Natalia M. Guerrero[13], Christopher E. Henze[17], Aleisha Hogan[28], Jonathan Horner[18], Chelsea X. Huang[13], Jonathan Irwin[6], Stephen R. Kane[29], John Kielkopf[30], Andrew W. Mann[31], Tsevi Mazeh[32], James McCormac[19], Curtis McCully[23,33], Matthew W. Mengel[18], Ismael Mireles[13], Jack Okumura[18], Peter Plavchan[34], Samuel N. Quinn[6], Markus Rabus[33,35], Sophie Saesen[3], Joshua E. Schlieder[36], Damien Segransan[3], Bernie Shiao[7], Avi Shporer[13], Robert J. Siverd[37], Keivan G. Stassun[38], Vincent Suc[1,39], Thiam-Guan Tan[40], Pascal Torres[2,11], Chris G. Tinney[41], Stephane Udry[3], Leonardo Vanzi[42,43], Michael Vezie[13], Jose I. Vines[44], Maja Vuckovic[45], Duncan J. Wright[18], Daniel A. Yahalomi[6], Abner Zapata[39,42,43], Hui Zhang[46], and Carl Ziegler[47]

[1] Facultad de Ingeniería y Ciencias, Universidad Adolfo Ibáñez, Av. Diagonal las Torres 2640, Peñalolén, Santiago, Chile; rafael.brahm@uai.cl
[2] Millennium Institute for Astrophysics, Chile
[3] Geneva Observatory, University of Geneva, Chemin des Maillettes 51, 1290 Versoix, Switzerland
[4] University of Southern Queensland, Centre for Astrophysics, Toowoomba, QLD 4350, Australia
[5] Department of Astronomy, Yale University, New Haven, CT 06511, USA
[6] Center for Astrophysics | Harvard & Smithsonian, 60 Garden St., Cambridge, MA 02138, USA
[7] Space Telescope Science Institute, 3700 San Martin Dr., Baltimore, MD 21218, USA
[8] European Southern Observatory, Alonso de Córdova 3107, Vitacura, Casilla 19001, Santiago, Chile
[9] Instituto de Astronomía, Universidad Católica del Norte, Angamos 0610, 1270709, Antofagasta, Chile
[10] Max-Planck-Institut für Astronomie, Königstuhl 17, Heidelberg D-69117, Germany
[11] Instituto de Astrofísica, Pontificia Universidad Católica de Chile, Av. Vicuña Mackenna 4860, Macul, Santiago, Chile
[12] School of Physics and Astronomy, Tel-Aviv University, Tel Aviv 69978, Israel
[13] Department of Physics and Kavli Institute for Astrophysics and Space Research, Massachusetts Institute of Technology, Cambridge, MA 02139, USA
[14] Department of Earth, Atmospheric and Planetary Sciences, Massachusetts Institute of Technology, Cambridge, MA 02139, USA
[15] Department of Aeronautics and Astronautics, MIT, 77 Massachusetts Ave., Cambridge, MA 02139, USA
[16] Department of Astrophysical Sciences, Princeton University, NJ 08544, USA[48]
[17] NASA Ames Research Center, Moffett Field, CA 94035, USA
[18] University of Southern Queensland, Centre for Astrophysics, West Street, Toowoomba, QLD 4350, Australia
[19] Dept. of Physics, University of Warwick, Gibbet Hill Road, Coventry CV4 7AL, UK
[20] Department of Astronomy, The University of Texas at Austin, TX 78712, USA
[21] Cerro Tololo Inter-American Observatory, Casilla 603, 1700000, La Serena, Chile
[22] University of Colorado/CASA, Boulder, CO 80309, USA
[23] Las Cumbres Observatory Global Telescope Network, Santa Barbara, CA 93117, USA
[24] Centre for Exoplanets and Habitability, University of Warwick, Gibbet Hill Rd., Coventry CV4 7AL, UK
[25] SETI Institute, Mountain View, CA, 94043, USA
[26] SETI Institute/NASA Ames Research Center, Moffett Field, CA 94035, USA
[27] NASA Exoplanet Science Institute/Caltech-IPAC, Pasadena, CA, USA
[28] School of Physics and Astronomy, University of Leicester, University Rd., Leicester LE1 7RH, UK
[29] Department of Earth and Planetary Sciences, University of California, Riverside, CA 92521, USA
[30] Department of Physics and Astronomy, University of Louisville, Louisville, KY 40292, USA
[31] Department of Physics and Astronomy, The University of North Carolina at Chapel Hill, Chapel Hill, NC 27599-3255, USA
[32] School of Physics and Astronomy, Raymond and Beverly Sackler Faculty of Exact Sciences, Tel Aviv University, Tel Aviv, 6997801, Israel
[33] Department of Physics, University of California, Santa Barbara, CA 93106-9530, USA
[34] George Mason University, 4400 University Dr. MS 3F3, Fairfax, VA 22030, USA
[35] Las Cumbres Observatory Global Telescope, 6740 Cortona Dr., Suite 102, Goleta, CA 93111, USA
[36] Exoplanets and Stellar Astrophysics Laboratory, Code 667, NASA Goddard Space Flight Center, Greenbelt, MD 20771, USA
[37] Gemini Observatory/NSF's NOIRLab, 670 N. A'ohoku Pl., Hilo, HI 96720, USA
[38] Vanderbilt University, Department of Physics & Astronomy, 6301 Stevenson Center Lane, Nashville, TN 37235, USA
[39] El Sauce Observatory, Chile
[40] Perth Exoplanet Survey Telescope, Perth, Australia
[41] Exoplanetary Science at UNSW, School of Physics, UNSW Sydney, NSW 2052, Australia
[42] Department of Electrical Engineering, Pontificia Universidad Católica de Chile, Av. Vicuña Mackenna 4860, 7820436 Macul, Santiago, Chile
[43] Center of Astro-Engineering UC, Pontificia Universidad Católica de Chile, Av. Vicuña Mackenna 4860, 7820436 Macul, Santiago, Chile
[44] Departamento de Astronomía, Universidad de Chile, Camino El Observatorio 1515, Las Condes, Santiago, Chile
[45] Instituto de Física y Astronomía, Universidad de Vaparaíso, Casilla 5030, Valparaíso, Chile

[46] School of Astronomy and Space Science, Key Laboratory of Modern Astronomy and Astrophysics in Ministry of Education, Nanjing University, Nanjing 210046, Jiangsu, People's Republic of China
[47] Dunlap Institute for Astronomy and Astrophysics, University of Toronto, 50 St. George St., Toronto, Ontario M5S 3H4, Canada
*Received 2020 August 4; revised 2020 September 10; accepted 2020 September 17; published 2020 October 29*

## Abstract

We present the discovery of two new 10 day period giant planets from the Transiting Exoplanet Survey Satellite mission, whose masses were precisely determined using a wide diversity of ground-based facilities. TOI-481 b and TOI-892 b have similar radii ($0.99 \pm 0.01\ R_J$ and $1.07 \pm 0.02\ R_J$, respectively), and orbital periods (10.3311 days and 10.6266 days, respectively), but significantly different masses ($1.53 \pm 0.03\ M_J$ versus $0.95 \pm 0.07\ M_J$, respectively). Both planets orbit metal-rich stars ([Fe/H] $= +0.26 \pm 0.05$ dex and [Fe/H] $= +0.24 \pm 0.05$ for TOI-481 and TOI-892, respectively) but at different evolutionary stages. TOI-481 is a $M_\star = 1.14 \pm 0.02\ M_\odot$, $R_\star = 1.66 \pm 0.02\ R_\odot$ G-type star ($T_{\rm eff} = 5735 \pm 72$ K), that with an age of 6.7 Gyr, is in the turn-off point of the main sequence. TOI-892 on the other hand, is a F-type dwarf star ($T_{\rm eff} = 6261 \pm 80$ K), which has a mass of $M_\star = 1.28 \pm 0.03\ M_\odot$ and a radius of $R_\star = 1.39 \pm 0.02\ R_\odot$. TOI-481 b and TOI-892 b join the scarcely populated region of transiting gas giants with orbital periods longer than 10 days, which is important to constrain theories of the formation and structure of hot Jupiters.

*Unified Astronomy Thesaurus concepts:* Exoplanet detection methods (489); Transit photometry (1709); Radial velocity (1332); Exoplanet astronomy (486)

*Supporting material:* machine-readable tables

## 1. Introduction

Among the vast diversity of extrasolar planets discovered throughout the past three decades, those known as hot Jupiters (e.g., Mayor & Queloz 1995) are arguably the most well-studied population. These objects are gas giant planets ($R_P \gtrsim 0.8\ R_J$) orbiting closely around their host stars, with typical orbital periods shorter than ≈10 days.

Despite having a relatively low occurrence rate of ≈1% (Wang et al. 2015; Zhou et al. 2019), due to strong observational biases favoring their detection and characterization, hot Jupiters represent ≈75% of the total sample of transiting extrasolar planets for which both masses and radii are determined with a precision of at least 20%.[49]

Follow-up observations of hot Jupiters have delivered significant scientific results—including the first studies on the atmospheres of planets outside our own solar system (e.g., Charbonneau et al. 2002; Vidal-Madjar et al. 2003; Pont et al. 2008) and significant misalignments between orbital and stellar spin axes (Queloz et al. 2010; Winn et al. 2010; Hébrard et al. 2011).

While in principle the large amount of information available for transiting hot Jupiters should help us in unveiling the formation and evolution mechanisms that allow the existence of close-in gas giants, their extreme environments produced by the proximity to the host stars makes the interpretation of hot Jupiter properties a challenging task (see Dawson & Johnson 2018, for a comprehensive review). The exact formation/migration mechanism of hot Jupiters (e.g., Wu & Lithwick 2011; Beaugé & Nesvorný 2012; Naoz et al. 2012) and the mechanism responsible for generating highly inflated radii (e.g., Bodenheimer et al. 2001; Batygin & Brown 2010; Leconte et al. 2010; Kurokawa & Inutsuka 2015) are some of the active challenges in the field.

Gas giants with orbital periods longer than that of typical hot Jupiters (often called warm Jupiters) should not be significantly influenced by these proximity effects, making the orbital and physical characterization of warm Jupiters an important step to solve some of the aforementioned challenges (e.g., Dong et al. 2014; Lopez & Fortney 2016; Thorngren et al. 2016). Ground-based photometric surveys (e.g., Bakos et al. 2004, 2013; Pollacco et al. 2006; Pepper et al. 2007), which have discovered the vast majority (≈80%) of bright transiting hot Jupiter systems, have strong limitations for discovering planets with periods longer than $P \gtrsim 8$ days (Gaudi et al. 2005). Space-based missions such as Kepler (Borucki et al. 2010), Kepler-K2 (Howell et al. 2014), and CoRoT (Auvergne et al. 2009) allowed the discovery and orbital characterization of the first two dozen of such systems (Bonomo et al. 2010; Deeg et al. 2010; Shporer et al. 2017; Almenara et al. 2018; Brahm et al. 2018; Jordán et al. 2019), but due to its significantly larger field of view, the Transiting Exoplanet Survey Satellite (TESS) mission (Ricker et al. 2015) is expected to significantly increase that number (Sullivan et al. 2015; Barclay et al. 2018). In just its first two years of operation, TESS has demonstrated its ability to discover transiting warm Jupiters suitable for characterization follow-up (Huber et al. 2019; Nielsen et al. 2019; Rodriguez et al. 2019; Addison et al. 2020; Gill et al. 2020), and this number will grow with the extended mission (Cooke et al. 2019).

Here we present the discovery and orbital characterization of two gas giants located in the relatively sparsely populated parameter space of orbital periods slightly longer than 10 days. These discoveries were realized in the context of the Warm gIaNts with tEss (WINE) collaboration, which focuses on the systematic characterization of TESS transiting warm giant planets (e.g., Brahm et al. 2019; Jordán et al. 2020).

The paper is structured as follows. In Section 2 we present the TESS data, and follow-up photometric and spectroscopic observations that allowed the discovery of both planets. In Section 3 we describe the routines adopted to estimate the stellar parameters of both host stars and the final physical and orbital parameters of TOI-481 b and TOI-892 b. Our findings are discussed in Section 4.

## 2. Observations

### 2.1. Transiting Exoplanet Survey Satellite

TOI-481 and TOI-892 were monitored by TESS during its first year of operation. TOI-481 was observed in short-cadence

[48] MTA Distinguished Guest Fellow, Konkoly Observatory, Hungary.
[49] Based on the catalog of the physical properties of transiting planetary systems (TEPCat; Southworth 2011), updated on 2020 July 7.

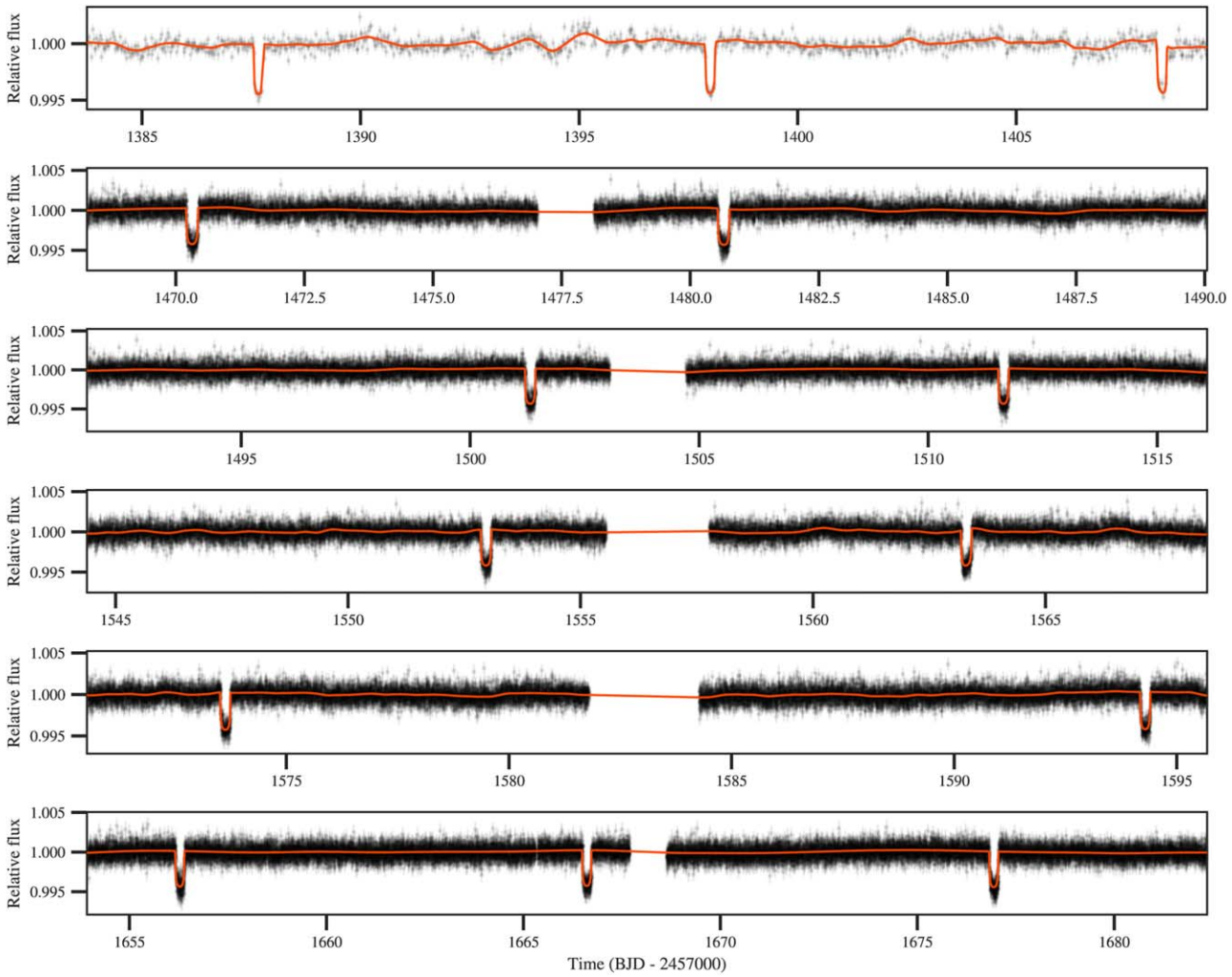


**Figure 1.** TOI-481 light curves of the six TESS sectors used in our analysis. The top panel presents the TESS Sector 3 data from the full-frame images as black points with error bars obtained with `tesseract` (see the text), while the rest of the panels show the 2 minute cadence pre-search data conditioning simple aperture photometry light curves for Sectors 6, 7, 9, 10, and 13, respectively. The orange line corresponds to the model obtained in Section 3, which consists of a transit model combined with a Gaussian process that describes the remaining flux variability.

(2 minutes) mode in Sectors 6, 7, 9, 10, and 13, and in long-cadence (30 minutes) mode in Sector 3. On the other hand, TOI-892 was only observed in Sector 6, in long-cadence mode. Transiting candidates were identified on both stars by the TESS Science Office, and were released as TESS Objects of Interest (TOI) to the community. TOI-481 b was identified as a candidate based on two clear transit-like features present in the Science Processing Operations Center (SPOC) light curve (Jenkins et al. 2016) of Sector 6. TOI-481 presented a strong detection at $68\sigma$ and passed all the diagnostic tests conducted and presented in the data validation report (Twicken et al. 2018; Li et al. 2019), including the odd/even transit depth test, and the difference image centroiding and ghost diagnostic tests (which help reject false positives due to background sources). No additional transit-like signals were identified in the light curve. On the other hand, TOI-892 b was reported as a TESS alert on 2019 July 12 based on the analysis of the quick look pipeline (Huang et al. 2019) of Sector 6. For both candidates the predicted planetary radii were consistent with being Jovian planets with orbital periods close to 10 days.

For the TOI-481 analysis presented in this study, we downloaded the pre-search data conditioning simple aperture photometry light curves (Stumpe et al. 2012) of Sectors 6, 7, 9, 10, and 13 from the Mikulski Archives for Space Telescopes (MAST; see Figure 1). Systematic trends were removed from these light curves using the co-trending basis vectors (Smith et al. 2012; Stumpe et al. 2014), generated by the TESS SPOC at NASA Ames Research Center. We additionally obtained the long-cadence light curve from the full-frame images of Sector 3 using the `tesseract`[50] pipeline. For the analysis of TOI-892, we generated the long-cadence light curve from the full-frame images of Sector 6 through `tesseract` (see Figure 2). The long-cadence light curves for TOI-481 and TOI-892 used in this study are listed in Table 1.

### 2.2. Ground-based Photometry

The limited spatial resolution of the TESS mission and its relatively large pixel scale ($21''\,\mathrm{pix}^{-1}$) makes necessary the execution of ground-based photometric observations to confirm that the transit features occur on target and not on close neighbor stars. Transits of both candidates were monitored with three different ground-based facilities installed in Chile. These

[50] https://github.com/astrofelipe/tesseract

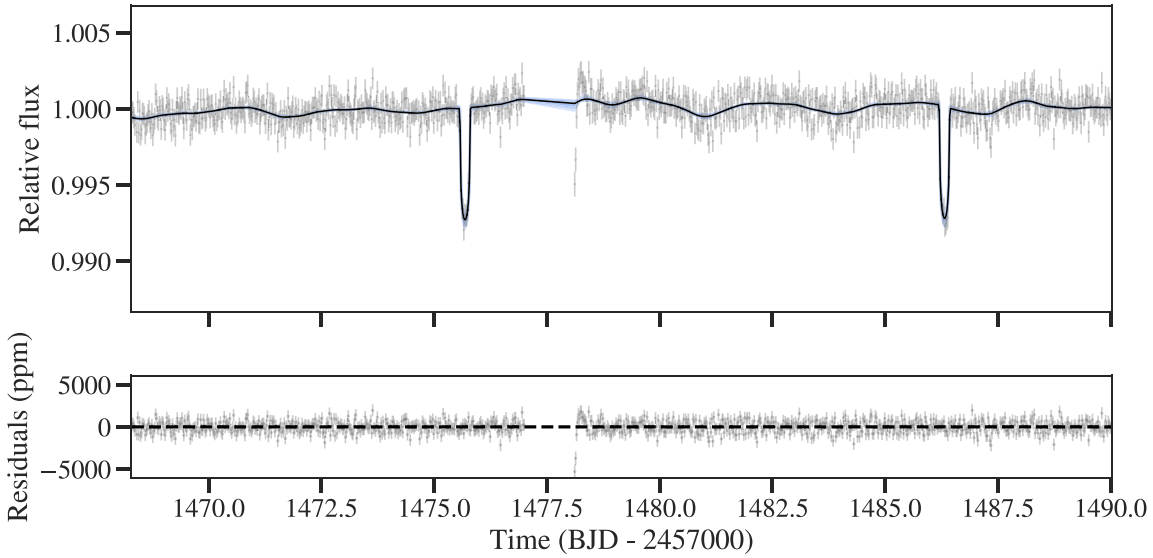


**Figure 2.** The top panel corresponds to the TESS 30 minute cadence light curve of TOI-892 generated through `tesseract` from the full-frame images of Sector 6. The solid line corresponds to the model generated from the posterior parameters of the analysis presented in Section 3. The bottom panel shows the residuals between the TESS light curve and the model.

**Table 1**
Long-cadence (30 Minutes) TESS Light Curve Data for TOI-481 and TOI-892 Obtained from the `tesseract` Extraction of the Full-frame Images of Sector 3 and 6, Respectively

| ID | BJD | Flux | $\sigma_{\rm Flux}$ | Sector |
|---|---|---|---|---|
| TOI-481 | 2458382.051879883 | 25279.4 | 4.8 | 3 |
| TOI-481 | 2458382.072692871 | 25272.1 | 4.7 | 3 |
| TOI-481 | 2458382.093566895 | 25274.6 | 4.7 | 3 |
| TOI-481 | 2458382.114379883 | 25282.0 | 4.7 | 3 |
| TOI-481 | 2458382.135192871 | 25279.4 | 4.7 | 3 |
| TOI-481 | 2458382.156066895 | 25277.6 | 4.7 | 3 |
| TOI-481 | 2458382.176940918 | 25283.0 | 4.7 | 3 |
| TOI-481 | 2458382.197753906 | 25282.9 | 4.7 | 3 |
| TOI-481 | 2458382.218566895 | 25277.7 | 4.7 | 3 |
| TOI-481 | 2458382.239440918 | 25299.6 | 4.7 | 3 |

(This table is available in its entirety in machine-readable form.)

observations were performed in the context of the TESS follow-up observing program (TFOP) working group subgroup 1 (SG1). The four photometric time series are publicly available on the exoplanet follow-up observing program for TESS (ExoFOP-TESS) website.[51]

#### 2.2.1. CHAT

The Chilean Hungarian Automated Telescope[52] (CHAT) is a robotic facility installed at Las Campanas Observatory in Chile. CHAT consists in a FORNAX 200 equatorial mount, and a 0.7 m telescope coupled to a FLI ML-23042 CCD of 2048 × 2048 pixels, which delivers a pixel scale of $0\farcs6\,{\rm pix}^{-1}$. CHAT contains a set of $i'$, $r'$, and $g'$ passband filters.

TOI-481 was observed with CHAT on the night of 2019 March 30 with the $i'$ filter adopting an exposure time of 20 s. We obtained 516 images of TOI-481 with airmass values between 1.2 and 2. CHAT data were processed with a dedicated pipeline that performs differential aperture photometry, where the optimal comparison sources and the radius of the photometric aperture are automatically selected (e.g., Espinoza et al. 2019a; Jones et al. 2019; Jordán et al. 2019). The light curve obtained is presented in the left panel of Figure 3 and shows an ingress for TOI-481 b which confirms that the transit identified in the TESS data occurs in a region of 8″ centered on TOI-481.

TOI-892 was photometrically monitored with CHAT on the night of 2019 November 27. The $i'$ filter was used to obtain 189 images with an exposure time of 66 s. The right panel of Figure 3 presents the CHAT light curve obtained for TOI-892 b, where a ≈7000 ppm egress can be identified, ensuring that the transit occurs inside 6″ from TOI-892.

#### 2.2.2. MEarth-South

The MEarth-South project (Irwin et al. 2015) consists in an array of eight identical robotic 0.4 m telescopes installed in the Cerro Tololo International Observatory, in Chile. Seven telescopes of the array were used to monitor a transit of TOI-892 b the night of 2020 February 20. Each of the telescopes obtained approximately 360 images with a cadence of 52 s using a custom-made RG715 filter. The data were processed with the MEarth-South pipeline producing the light curve displayed in Figure 3, which further confirms the occurrence of the transit on the target by registering an ingress.

#### 2.2.3. Next Generation Transit Survey

The Next Generation Transit Survey (NGTS; Wheatley et al. 2018) is an array of 12 identical robotic telescopes installed at the Paranal Observatory in Chile. Four NGTS telescopes were used simultaneously on the night of 2019 December 3 to monitor an egress of TOI-481 b. Exposures were taken using a custom NGTS filter (520–890 nm) with 10 s exposure times which resulted in a ∼12 s cadence. Data were reduced using the NGTS aperture photometry pipeline detailed in Bryant et al. (2020). The NGTS light curve is presented in Figure 3.

[51] https://exofop.ipac.caltech.edu/tess
[52] https://www.exoplanetscience2.org/sites/default/files/submission-attachments/poster_aj.pdf

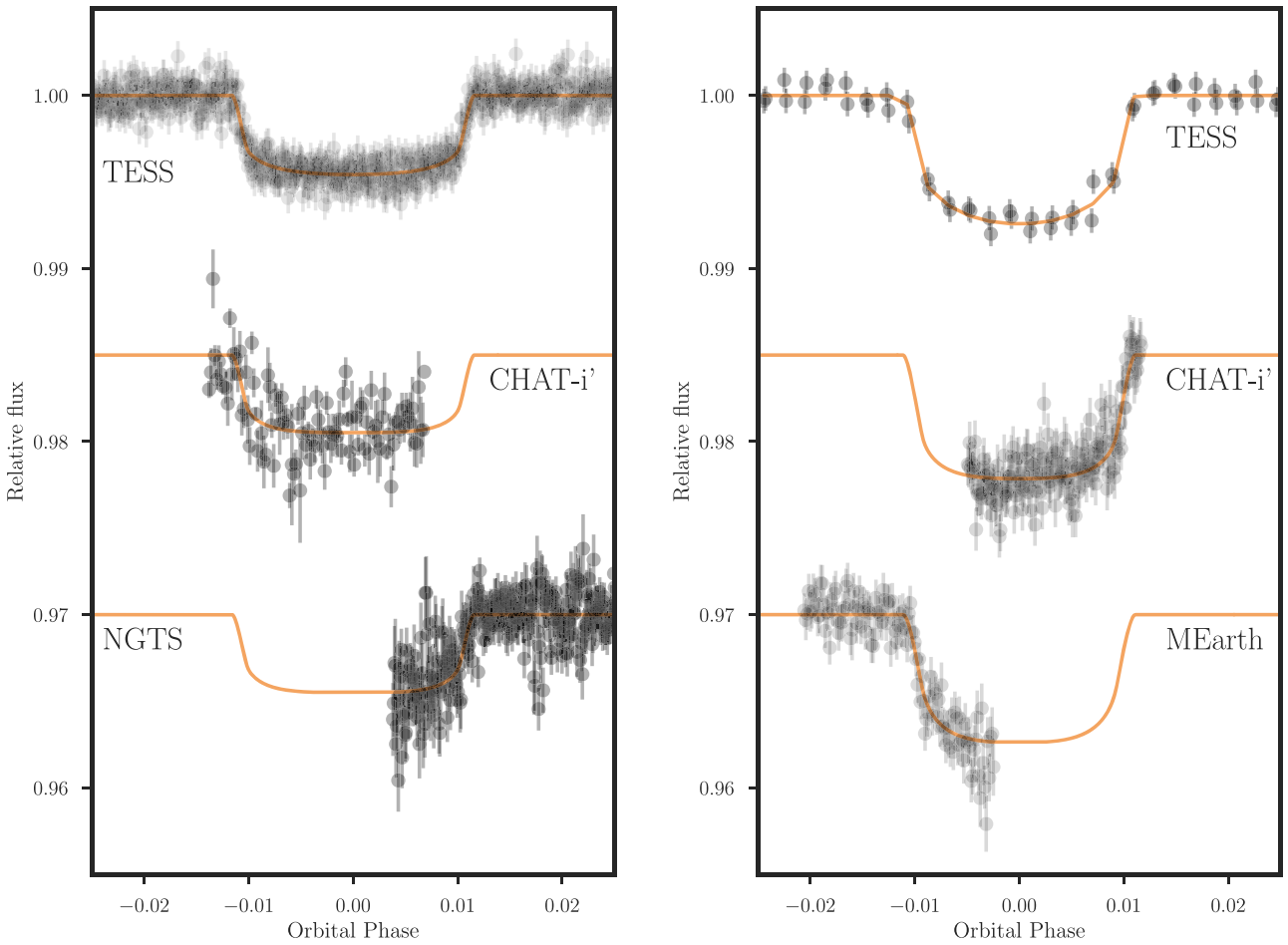


**Figure 3.** The left panel shows the phase-folded 2 minute cadence TESS photometry of TOI-481 along with the ground-based follow-up light curves of CHAT and NGTS. The solid line shows the corresponding transit model in each case. The right panel shows the phase-folded TESS long cadence, CHAT, and MEarth light curves for TOI-892.

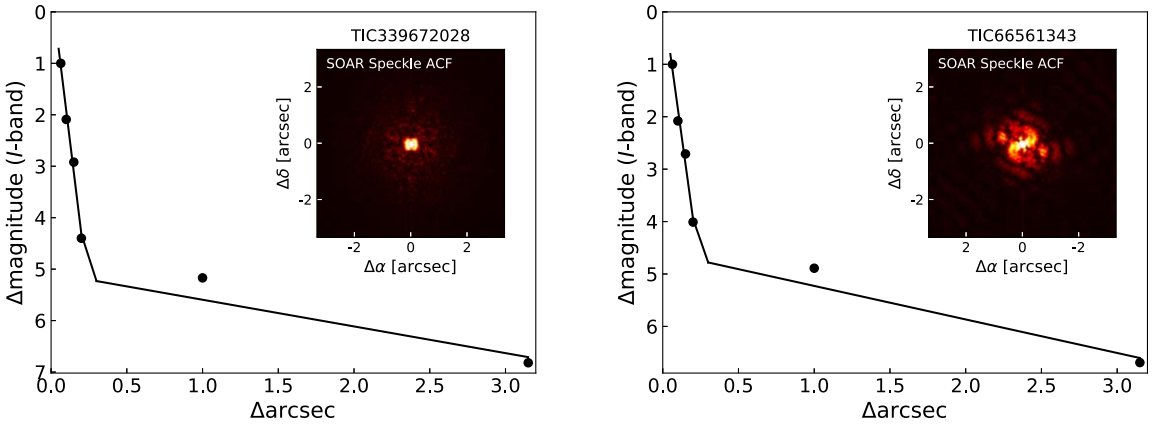


**Figure 4.** Contrast curve plots and autocorrelation functions from Speckle imaging in the *I* band using the HRcam at SOAR, for TOI-481 (left panel) and TOI-892 (right panel). The black points correspond to the $5\sigma$ contrast curve for each star. The solid line is the linear fit to the data for separations $<0\farcs2$ and $>0\farcs2$.

### *2.3. High-resolution Imaging*

The identification of contaminating sources in the neighborhood of transiting candidates is important for constraining false-positive scenarios and for determining possible dilutions of the transits. In this context, TOI-481 and TOI-892 were imaged with the High-Resolution Camera (HRCam) installed at the 4.1m Southern Astrophysical Research (SOAR; Tokovinin 2018) telescope in Cerro Pachón, Chile. Observations took place on the night of 2019 November 9, in the context of the SOAR TESS Survey (Ziegler et al. 2020). No nearby sources were detected in the vicinity of either star (see Figure 4).

We also used the Gaia DR2 catalog (Gaia Collaboration et al. 2018) to identify the presence of close companions that

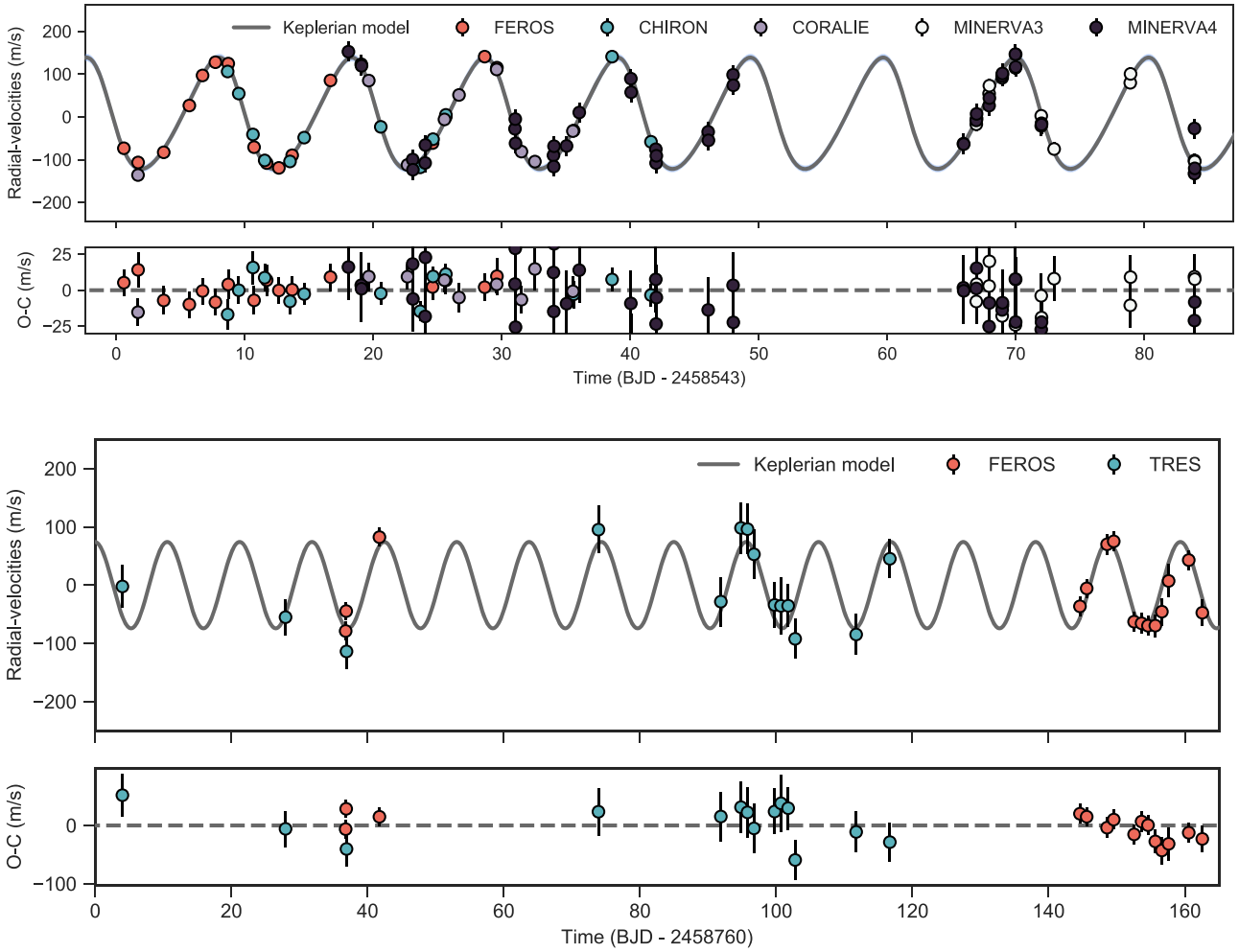


**Figure 5.** Radial velocity observations for TOI-481 (top panel) and TOI-892 (bottom panel). The solid line corresponds to a Keplerian model using the posterior parameters of the global modeling presented in Section 3. The residuals are also presented below the radial velocity curves for each system. The radial velocity measurements for NRES have been excluded from the plots due to their significantly larger error bars.

could dilute the transit depths of TOI-481 b and TOI-892 b obtained from the ground-based light curves presented in Section 2.2. We find that inside 10″ from the target, TOI-481 contains just one source having a magnitude difference of 8.7 mag in the *G* passband filter, which is too faint to significantly affect the transit depth of TOI-481 b. TOI-892 reports no nearby sources closer than 10″ to it.

### 2.4. High-resolution Spectroscopy

TOI-481 and TOI-892 were monitored with seven different spectrographs with the goal of measuring radial velocity variations to confirm the planetary nature of the transiting candidates and constrain their orbital parameters and masses. These observations are described in the following paragraphs and the radial velocities are presented in Table 2 and displayed in Figure 5.

#### 2.4.1. Fiber-fed Extended Range Optical Spectrograph

The Fiber-fed Extended Range Optical Spectrograph (FEROS; Kaufer et al. 1999) has a resolving power of $R = 48{,}000$ and is installed on the MPG2.2 m telescope at La Silla Observatory in Chile. For this study, all FEROS data were processed with the CERES pipeline (Brahm et al. 2017a), which delivers optimally extracted, wavelength calibrated, and instrumental drift corrected spectra, along with the radial velocity and bisector span measurements.

We obtained 16 spectra with FEROS of TOI-481 over a time span of 30 days starting on the night of 2019 February 28. We adopted an exposure time of 300 s which generated spectra with a signal-to-noise ratio per resolution element of ∼110.

**Table 2**
Radial Velocity Measurements for TOI-481 and TOI-892

| ID | BJD −2450000 | RV (m s$^{-1}$) | $\sigma_{RV}$ (m s$^{-1}$) | Instrument |
|---|---|---|---|---|
| TOI-481 | 8543.59063 | 37723.80 | 5.40 | FEROS |
| TOI-481 | 8544.41789 | 37227.70 | 41.69 | NRES |
| TOI-481 | 8544.43251 | 37253.27 | 143.99 | NRES |
| TOI-481 | 8544.44711 | 37203.45 | 123.13 | NRES |
| TOI-481 | 8544.69135 | 37672.30 | 9.40 | CORALIE |
| TOI-481 | 8544.69945 | 37690.60 | 9.40 | FEROS |
| TOI-481 | 8545.41809 | 37032.61 | 120.31 | NRES |
| TOI-481 | 8545.43966 | 37015.83 | 72.10 | NRES |
| TOI-481 | 8546.69284 | 37714.30 | 6.30 | FEROS |
| TOI-481 | 8548.68585 | 37823.70 | 5.50 | FEROS |

(This table is available in its entirety in machine-readable form.)

For TOI-892 we obtained 15 FEROS spectra between 2019 November 9 and 2020 March 14. In this case the exposure time was 900 s and the obtained spectra reached a typical signal-to-noise ratio per resolution element of ∼80.

In both cases we used the simultaneous calibration technique by taking a spectrum of a Thorium–Argon lamp with the comparison fiber to trace the instrumental drift during the science exposure.

#### 2.4.2. CHIRON

The CHIRON instrument (Tokovinin et al. 2013) is a high-resolution and fiber-fed spectrograph mounted on the 1.5 m Smarts telescope at the Cerro Tololo Inter-American Observatory (CTIO), Chile. We collected a total of 13 spectra of TOI-481 with CHIRON, between 2019 March 8 and April 10. For this object we used the image slicer mode ($R = 80{,}000$), with exposure times between 750 and 1200 s, leading to a mean signal-to-noise per pixel of 33. From this dataset, we computed precision radial velocities following the method described in Wang et al. (2019), Jones et al. (2019), and Jordán et al. (2020). We achieve a mean radial velocity precision of 9 m s$^{-1}$.

#### 2.4.3. Tillinghast Reflector Echelle Spectrograph

The Tillinghast Reflector Echelle Spectrograph (TRES; Fűrész 2008)[53] is a $R = 44{,}000$ fiber-fed instrument mounted on the 1.5 m Tillinghast Reflector at the Fred L. Whipple Observatory (FLWO) on Mt. Hopkins, Arizona. TRES was used to obtain 14 spectra of TOI-892 between 2019 October 7 and 2020 January 28. A full description of the reduction pipeline and radial velocity extraction process can be seen in Buchhave et al. (2010). We deviate from this methodology in the creation of the reference template used for the cross-correlation. We created a high signal-to-noise template spectrum by shifting and median-combining all the spectra, and cross-correlating each observed spectrum against this template to determine the final radial velocities.

The TRES spectra of TOI-892 were analyzed using the stellar parameter classification (SPC) package (Buchhave et al. 2012). From this analysis, we estimated the effective temperature, metallicity, surface gravity, and rotational velocity of TOI-892 to be: $T_{\rm eff} = 6048 \pm 50$ K, $\log g_\star = 4.32 \pm 0.11$ dex, $[{\rm Fe/H}] = +0.32 \pm 0.08$ dex, and $v \sin i = 8.2 \pm 0.5$ km s$^{-1}$.

#### 2.4.4. CORALIE

CORALIE is a high-resolution ($R = 60{,}000$) fiber-fed spectrograph mounted on the 1.2 m Swiss Euler telescope at La Silla Observatory, Chile. CORALIE is a stabilized instrument with a comparison fiber to trace the instrumental variations during scientific exposures. We obtained nine CORALIE spectra of TOI-481 between 2019 March 1 and April 4 using a Fabry–Perot as a wavelength comparison source. The CORALIE data were processed with its standard data reduction software, where radial velocities and line bisector spans are computed via cross-correlation with a G2 binary mask. In an exposure time of 1200–1800 s we obtain signal-to-noise ratio per resolution element of about 30 in individual spectra, corresponding to a final radial velocity uncertainty of ∼10 m s$^{-1}$.

[53] http://www.sao.arizona.edu/html/FLWO/60/TRES/GABORthesis.pdf

#### 2.4.5. MINERVA-Australis

MINERVA-Australis is an array of four PlaneWave CDK700 telescopes which can be simultaneously fiber-fed to a single KiwiSpec R4-100 high-resolution ($R = 80{,}000$) spectrograph (Barnes et al. 2012; Addison et al. 2019, 2020). TOI-481 was monitored by MINERVA-Australis using one and/or two telescopes in the array (MINERVA3 and MINERVA4) between 2019 March 1 and May 23, obtaining 54 spectra in the process over 22 different epochs. Radial velocities for the observations are derived for each telescope by cross-correlation, where the template being matched is the mean spectrum of each telescope. The instrumental variations are corrected using simultaneous Thorium–Argon arc lamp observations. Radial velocities computed from different MINERVA telescopes are modeled in Section 3.3 as originating from independent instruments.

#### 2.4.6. Network of Robotic Echelle Spectrographs

Las Cumbres Observatory's (Brown et al. 2013) Network of Robotic Echelle Spectrographs (NRES; Siverd et al. 2018) is a global array of echelle spectrographs mounted on 1 m telescopes, with a resolving power of $R \approx 53{,}000$. TOI-481 was observed with the NRES node located at the South African Astronomical Observatory, for nine nights between 2019 March and April. At each observing epoch, two or three consecutive exposures were obtained with a total nightly exposure time of 3600 s. Overall, 21 spectra were obtained, with an individual signal-to-noise ratio per resolution element larger than 30.

A SpecMatch (Yee et al. 2017) analysis was performed on the NRES spectra and yielded $T_{\rm eff} = 5730 \pm 100$ K, $\log g = 3.9 \pm 0.1$ dex, $[{\rm Fe/H}] = +0.34 \pm 0.06$ dex, and $v \sin i \lesssim 2$ km s$^{-1}$. The radial velocity of each exposure was derived via cross-correlation with a PHOENIX template (Husser et al. 2013) with $T_{\rm eff} = 5700$ K, $\log g = 4.0$ dex, $[{\rm Fe/H}] = +0.5$ dex, and $v \sin i = 2$ km s$^{-1}$. Systematic drifts were corrected per order (e.g., Engel et al. 2017).

## 3. Analysis

### 3.1. Properties of the Host Star

We used the co-added FEROS spectra of TOI-481 and TOI-892 to obtain their respective atmospheric parameters. They were obtained using the ZASPE code (Brahm et al. 2017b). ZASPE works by comparison via $\chi^2$ minimization of the observed spectrum with a grid of synthetic models generated from the ATLAS9 model atmospheres (Castelli & Kurucz 2003). The evaluation is performed in a subset of spectral regions that are most sensitive to changes in the atmospheric parameters. The errors on the atmospheric parameters are computed through Monte Carlo simulations where the depth of the absorption lines of the synthetic models are randomly perturbed to account for the systematic model mismatch. For TOI-481 we obtain an effective temperature of $T_{\rm eff} = 5735 \pm 72$ K, a surface gravity of $\log g = 4.06^{+0.01}_{-0.01}$ dex, a metallicity of $[{\rm Fe/H}] = +0.26 \pm 0.05$ dex, and a projected rotational velocity of $v \sin i = 4.54 \pm 0.3$ km s$^{-1}$. On the other hand, for TOI-892 we found the following set of atmospheric parameters: $T_{\rm eff} = 6261 \pm 80$ K, $\log g = 4.26^{+0.02}_{-0.02}$ dex, $[{\rm Fe/H}] = +0.24 \pm 0.05$ dex, and $v \sin i = 7.69 \pm 0.5$ km s$^{-1}$.

For estimating the stellar physical parameters we followed the same procedure presented in Brahm et al. (2019). Briefly, we use the PARSEC isochrones (Bressan et al. 2012) containing the

**Table 3**
Stellar Properties of TOI-481 and TOI-892

| Parameter | TOI-481 | TOI-892 | References |
|---|---|---|---|
| Names | | | |
| | TIC 339672028 | TIC 66561343 | TICv8 |
| | 2MASS J07220299-5723054 | UCAC4 394-009979 | 2MASS |
| | TYC 8559-00623-1 | TYC 5351-00283-1 | TYCHO |
| R.A. (J2015.5) | $07^h22^m03^s.04$ | $05^h46^m57^s.17$ | TICv8 |
| Decl. (J2015.5) | $-57^d23^m05.99a$ | $-11^d14^m07^s.22$ | TICv8 |
| $pm^{R.A.}$(mas yr$^{-1}$) | 25.68 ± 0.06 | −0.14 ± 0.09 | Gaia DR2 |
| $pm^{decl.}$ (mas yr$^{-1}$) | −25.38 ± 0.08 | 5.97 ± 0.10 | Gaia DR2 |
| $\pi$ (mas) | 5.55 ± 0.03 | 2.91 ± 0.04 | Gaia DR2 |
| $T$ (mag) | 9.393 ± 0.006 | 10.974 ± 0.030 | TICv8 |
| $B$ (mag) | 10.68 ± 0.05 | 12.06 ± 0.04 | APASS (a) |
| $V$ (mag) | 10.04 ± 0.02 | 11.45 ± 0.02 | APASS |
| $G$ (mag) | 9.846 ± 0.002 | 11.343 ± 0.002 | Gaia DR2 (b) |
| $G_{BP}$ (mag) | 10.219 ± 0.005 | 11.643 ± 0.005 | Gaia DR2 |
| $G_{RP}$ (mag) | 9.354 ± 0.004 | 10.907 ± 0.003 | Gaia DR2 |
| $J$ (mag) | 8.80 ± 0.02 | 10.46 ± 0.03 | 2MASS (c) |
| $H$ (mag) | 8.48 ± 0.04 | 10.19 ± 0.02 | 2MASS |
| $K_s$ (mag) | 8.443 ± 0.02 | 10.11 ± 0.02 | 2MASS |
| $T_{\rm eff}$(K) | 5735 ± 72 | 6261 ± 80 | This work |
| log $g$(dex) | $4.06^{+0.01}_{-0.01}$ | $4.26^{+0.02}_{-0.02}$ | This work |
| [Fe/H](dex) | +0.26 ± 0.05 | +0.24 ± 0.05 | This work |
| $v \sin i$(km s$^{-1}$) | 4.54 ± 0.3 | 7.69 ± 0.5 | This work |
| $M_\star(M_\odot)$ | $1.14^{+0.02}_{-0.01}$ | $1.28^{+0.03}_{-0.02}$ | This work |
| $R_\star(R_\odot)$ | $1.66^{+0.02}_{-0.02}$ | $1.39^{+0.02}_{-0.02}$ | This work |
| $L_\star$ ($L_\odot$) | $2.72^{+0.10}_{-0.08}$ | $2.7^{+0.1}_{-0.1}$ | This work |
| $A_V$ (mag) | $0.06^{+0.05}_{-0.04}$ | $0.18^{+0.07}_{-0.08}$ | This work |
| Age (Gyr) | $6.7^{+0.4}_{-0.6}$ | $2.2^{+0.5}_{-0.5}$ | This work |
| $\rho_\star$ (g cm$^{-3}$) | $0.36^{+0.01}_{-0.01}$ | $0.67^{+0.04}_{-0.03}$ | This work |

**References.** (a) Munari et al. (2014); (b) Gaia Collaboration et al. (2018); (c) Skrutskie et al. (2006).

Gaia ($G$, $G_{BP}$, $G_{RP}$) and Two Micron All-Sky Survey (2MASS) absolute magnitudes for a given set of stellar mass, age, and metallicity. We then use the spectroscopic temperature, the observed magnitudes, and the Gaia parallax as data to estimate the stellar mass and the age of each system through a Monte Carlo Markov Chain (MCMC) exploration of the parameter space. We fix the metallicity of the isochrones to the value obtained with ZASPE. With this procedure for TOI-481 we obtained a mass of $M_\star = 1.14^{+0.02}_{-0.01}\ M_\odot$, a stellar radius of $R_\star = 1.66^{+0.02}_{-0.02}\ R_\odot$, and an age of $6.7^{+0.4}_{-0.6}$ Gyr. These parameters indicate that TOI-481 is in the final stages of its main-sequence lifetime, about to exhaust the hydrogen in its core. In the case of TOI-892 we obtained a mass of $M_\star = 1.28^{+0.03}_{-0.02}\ M_\odot$, a stellar radius of $R_\star = 1.39^{+0.02}_{-0.02}\ R_\odot$, and an age of $2.2^{+0.5}_{-0.5}$ Gyr. TOI-892 is therefore a metal-rich main-sequence F-type star. We stress that the uncertainties reported for the stellar physical parameters are internal, and do not account for possible systematic errors associated to the theoretical isochrones.

All atmospheric and physical parameters for both stars are presented in Table 3 along with their photometric magnitudes and other observable properties. Additionally, Figure 6 shows how the distributions for the stellar radius and effective temperature compared to the PARSEC stellar evolutionary models.

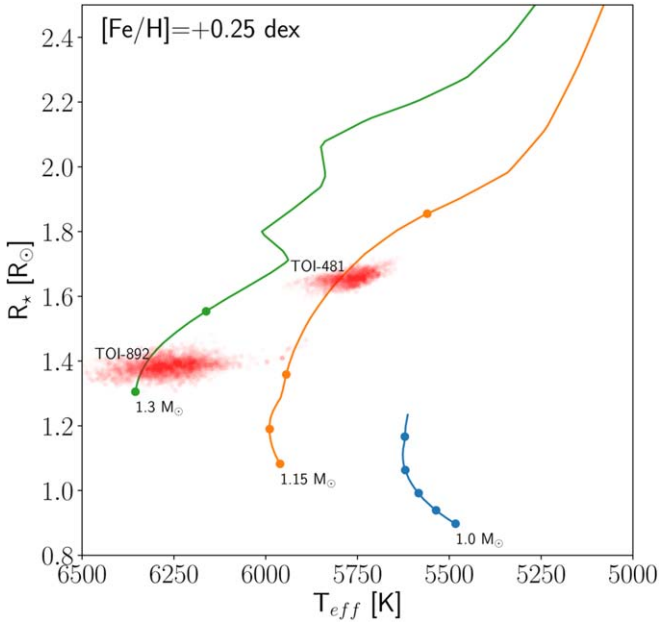


**Figure 6.** Posterior distributions for the effective temperature and stellar radius of TOI-481 and TOI-892 (red clumps). The lines represent PARSEC stellar evolutionary tracks for stellar masses of 1 $M_\odot$ (blue), 1.15 $M_\odot$ (orange), and 1.3 $M_\odot$ (green). A metallicity of [Fe/H] = +0.25 is assumed for the three evolutionary tracks, and the circles from bottom to top correspond of the ages of 1, 3, 5, and 7 Gyr.

We also applied the routines presented in Stassun et al. (2018a, 2018b) to obtain an independent set of stellar parameters for TOI-481 and TOI-892. Here we used the Gaia DR2 parallax, along with the *BVgri* magnitudes from the AAVSO Photometric All-Sky Survey (APASS), the $JHK_S$ magnitudes from 2MASS, the W1–W4 magnitudes from the Wide-field Infrared Survey Explorer (WISE), and the $G$, $G_{BP}$, $G_{RP}$ magnitudes from Gaia, to perform a spectral energy distribution fit. This method allows us to determine the stellar radius, metallicity, effective temperature, and surface gravity. All parameters obtained through this method are consistent at 1$\sigma$ to those listed in Table 3.

### 3.2. Radial Velocities

We analyzed the radial velocity time series of both systems to identify variations consistent with the presence of orbiting planets having the periodicity of the transiting candidates. We computed the generalized Lomb–Scargle periodograms by combining the radial velocities of different instruments for each system. The periodograms are presented in Figure 7 which confirm that both radial velocity sets have significant periodicity at the orbital period of the transiting candidate. The semi-amplitude of these periodic radial velocity variations is consistent with that of giant planets in moderately close-in orbits ($K \sim 100$ m s$^{-1}$).

In order to further confirm that the radial velocity signals are produced by orbiting planets, we analyzed the degree of correlation between the radial velocities and line bisector span measurements. We computed the Pearson correlation coefficient with errors through bootstrap finding $\rho_{\rm P} = 0.22 \pm 0.19$ and $\rho_{\rm P} = -0.19 \pm 0.25$ for TOI-481 b and TOI-892 b,

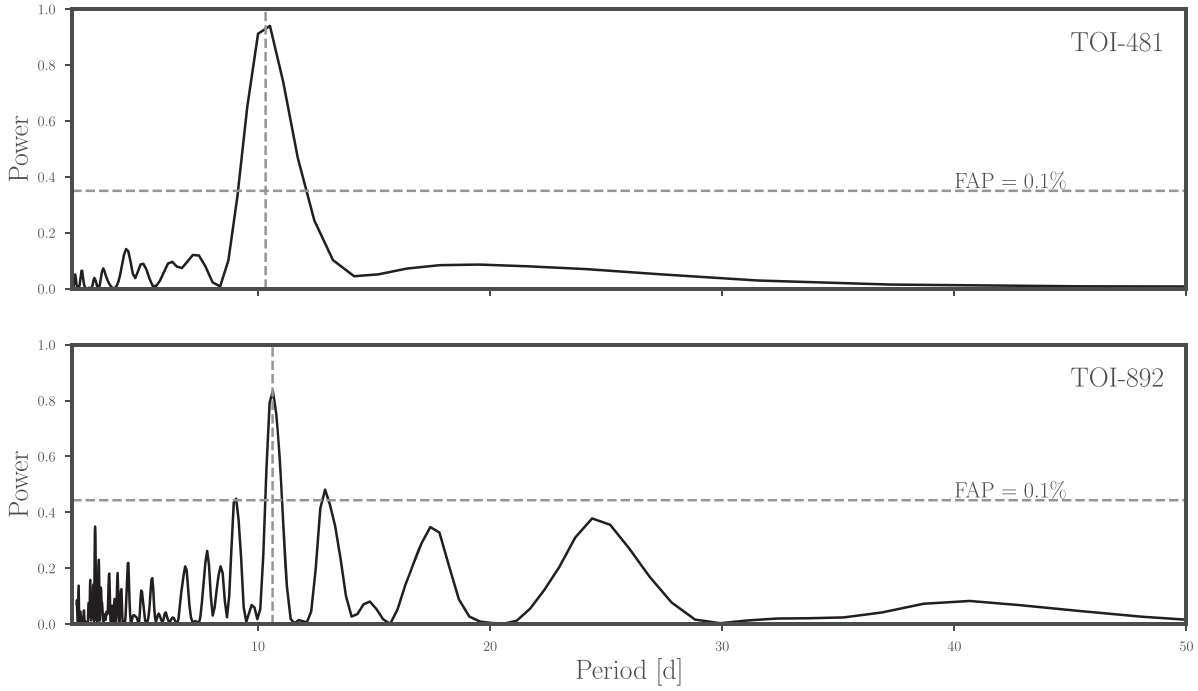


**Figure 7.** Lomb–Scargle periodograms for the radial velocity time series of TOI-481 (top panel) and TOI-892 (bottom panel). The horizontal dashed line corresponds to the 0.1% false-alarm probability. The vertical dashed line corresponds to the period of the transiting candidates.

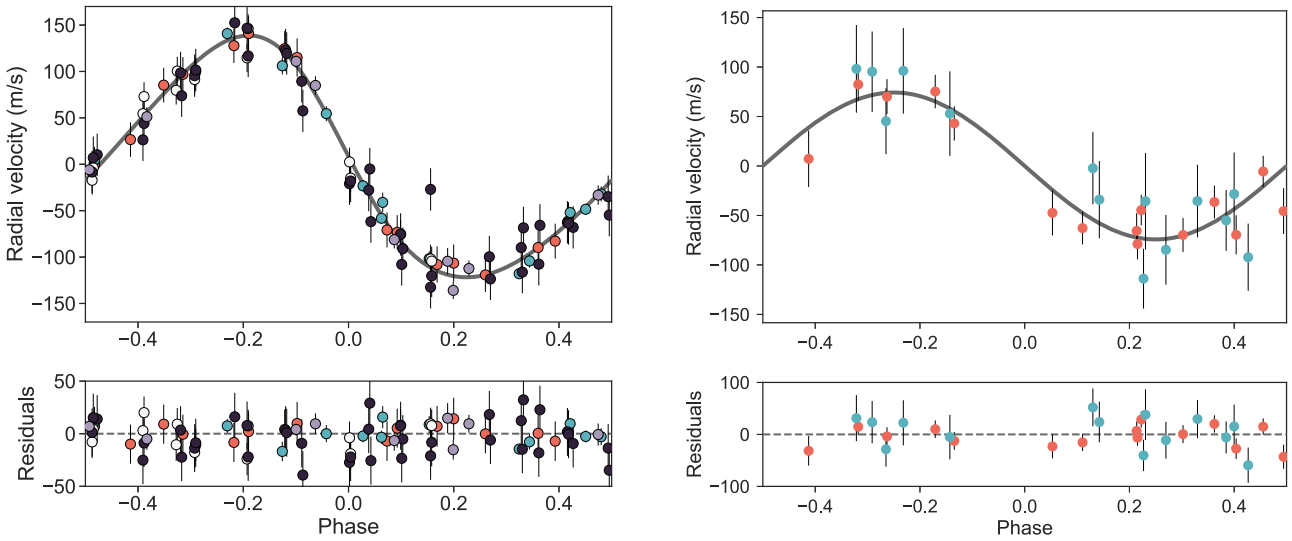


**Figure 8.** The left panel shows the radial velocities of TOI-481 b as a function of the orbital phase. The black line represents the model generated from the posterior distributions obtained in Section 3. The error bars include the jitter term obtained from the global analysis. The different colors represent the different instruments that were used, namely: FEROS (orange), CHIRON (blue), CORALIE (gray), MINERVA-3 (white), and MINERVA-4 (black). The right panel shows the same but for the FEROS (orange) and TRES (green) velocities of TOI-892 b.

respectively. Therefore, the absence of significant correlation between radial velocities and line bisector span measurements further supports the hypothesis that the radial velocity variations for both systems are produced by the gravitational pull of transiting giant planets.

### 3.3. Global Modeling

The global modeling of the photometric data and radial velocities for the TOI-481 and TOI-892 systems was performed with the `juliet` package (Espinoza et al. 2019a). This package can use either MultiNest (Feroz et al. 2009) through the PyMultiNest package (Buchner et al. 2014) or `dynesty` (Speagle 2020) to perform the posterior sampling via nested sampling algorithms, in order to also compute model comparison through Bayesian model evidences. `juliet` uses `batman` (Kreidberg et al. 2015) to model the photometric transits, while radial velocity variations are modeled with the `radvel` package (Fulton et al. 2018).

The parameters that were considered for modeling each system are described in the following paragraphs. The photometric and

phase-folded radial velocity models that were obtained with this process are presented in Figures 3 and 8, respectively, along with the corresponding observations.

### 3.3.1. Global Modeling of the TOI-481 System

For the TOI-481 system, we ran `juliet` fits using `dynesty`, as the number of free parameters (54) needed to account for the global fit is relatively large. In this global fit, we used the Espinoza (2019b) parameterization to fit for the planet-to-star radius ratio and the impact parameter. On top of this, we used a prior on the stellar density given by our analysis of the stellar properties in the previous subsection.

For the TESS photometry we used a Matérn 3/2 kernel implemented via `celerite` (Foreman-Mackey et al. 2017) to model systematic trends with individual hyperparameters for the amplitude and timescale of the process for each TESS sector. For the limb-darkening, we assumed a quadratic limb-darkening law parametrized using the noninformative sampling scheme outlined in Kipping (2013). For the short-cadence photometry we assumed unitary dilution factors, as these are already accounted for by the pre-search data conditioning algorithm. For the long-cadence photometry of Sector 3 that was extracted with our own aperture photometry, we considered a dilution factor with a prior between 0.95 and 1. We included photometric jitter terms for each sector, but the measured jitter was consistent with zero for all but Sector 3. We therefore only fit for photometric jitter in Sector 3 data.

For the CHAT and NGTS photometry, we found no evidence of obvious systematic trends and thus decided to model those data sets as having white-Gaussian noise. We used a linear limb-darkening law for both ground-based light curves and we fit for a dilution factor term in the case of the NGTS photometry.

Finally, for the radial velocities we used simple white-Gaussian noise models, where each instrument has its own systemic velocity and jitter term. Fits using both eccentric and non-eccentric orbits were performed, with the eccentric model being drastically preferred over the non-eccentric model ($\ln Z > 5$ in favor of the eccentric model). The final posterior parameters of the global analysis of TOI-481 b are presented in Table 4, along with the prior distributions used for each parameter.

By combining the stellar properties of TOI-481 with the posterior parameters of the adopted `juliet` fit, we find that TOI-481 b has a mass of $M_P = 1.53^{+0.03}_{-0.03}$ $M_J$, a radius of $R_P = 0.99^{+0.01}_{-0.01}$ $R_J$, a time-averaged equilibrium temperature (Méndez & Rivera-Valentín 2017) of $T_{eq} = 1370^{+10}_{-10}$ K (partial heat distribution of $\beta = 0.5$ and bond Albedo $A = 1$), and an orbital eccentricity of $e = 0.153^{+0.006}_{-0.007}$.

### 3.3.2. Global Modeling of the TOI-892 System

For the TOI-892 system we ran two `juliet` fits using PyMultiNest, as the number of free parameters (19) is much smaller in this case; one with the eccentricity and argument of the periastron as free parameters, and another one with those values fixed to zero. In both cases for modeling the `tesseract` light curve we adopted the quadratic law for the limb-darkening, and a Gaussian process with a Matern 3/2 Kernel to model the out-of-transit variations. For the MEarth and CHAT light curves we adopted a linear limb-darkening law. For the radial velocities we considered independent zero-points and jitter terms for each

**Table 4**
Prior and Posterior Parameters of the Global Analysis of TOI-481 b

| Parameter | Prior | Value |
|---|---|---|
| $P$ (days) | $N(10.331, 0.1)$ | $10.33111^{+0.00002}_{-0.00002}$ |
| $T_0$ (BJD) | $N(2458511.641, 0.1)$ | $2458511.6418^{+0.0002}_{-0.0002}$ |
| $\rho_\star$ (g cm$^{-3}$) | $U(0.36, 0.01)$ | $12.52^{+0.03}_{-0.04}$ |
| $r1$[a] | $U(0, 1)$ | $0.32^{+0.04}_{-0.04}$ |
| $r2$[a] | $U(0, 1)$ | $0.1228^{+0.0005}_{-0.0004}$ |
| $K$ (m s$^{-1}$) | $U(0, 1000)$ | $130.3^{+1.4}_{-1.4}$ |
| $\sqrt{e}\sin\omega$ | $U(-1, 1)$ | $0.354^{+0.009}_{-0.010}$ |
| $\sqrt{e}\cos\omega$ | $U(-1, 1)$ | $0.17^{+0.01}_{-0.01}$ |
| $q_1^{TESS}$ | $U(0, 1)$ | $0.64^{+0.06}_{-0.06}$ |
| $q_2^{TESS}$ | $U(0, 1)$ | $0.11^{+0.03}_{-0.03}$ |
| $q_1^{CHAT}$ | $U(0, 1)$ | $0.55^{+0.08}_{-0.08}$ |
| $q_1^{NGTS}$ | $U(0, 1)$ | $0.96^{+0.003}_{-0.04}$ |
| $\sigma_w^{TESS-S3}$ (ppm) | $LU(10^{-2}, 10^3)$ | $459^{+8}_{-9}$ |
| $\sigma_w^{CHAT}$ (ppm) | $LU(10^{-2}, 10^4)$ | $2815^{+95}_{-96}$ |
| mflux$^{TESS-S3}$ | $N(0, 0.1)$ | $-0.00001^{+0.00005}_{-0.00005}$ |
| mflux$^{TESS-S6}$ | $N(0, 0.1)$ | $-0.0000006^{+0.00005}_{-0.00005}$ |
| mflux$^{TESS-S7}$ | $N(0, 0.1)$ | $0.00001^{+0.00004}_{-0.00004}$ |
| mflux$^{TESS-S9}$ | $N(0, 0.1)$ | $-0.00004^{+0.00003}_{-0.00002}$ |
| mflux$^{TESS-S10}$ | $N(0, 0.1)$ | $-0.00003^{+0.00003}_{-0.00003}$ |
| mflux$^{TESS-S13}$ | $N(0, 0.1)$ | $0.001^{+0.004}_{-0.001}$ |
| mflux$^{CHAT}$ | $N(0, 0.1)$ | $-0.0019^{+0.0001}_{-0.0002}$ |
| mflux$^{NGTS}$ | $N(0, 0.1)$ | $0.00004^{+0.00007}_{-0.00007}$ |
| dilution$^{TESS-S3}$ | $U(0.95, 1.0)$ | $0.982^{+0.004}_{-0.005}$ |
| dilution$^{NGTS}$ | $U(0.95, 1.0)$ | $0.995^{+0.003}_{-0.003}$ |
| $\gamma_{CHIRON}$ (m s$^{-1}$) | $N(0, 50)$ | $41.1^{+1.4}_{-1.3}$ |
| $\gamma_{CORALIE}$ (m s$^{-1}$) | $N(37800, 50)$ | $37808.2^{+2.2}_{-2.2}$ |
| $\gamma_{FEROS}$ (m s$^{-1}$) | $N(37800, 50)$ | $37797.1^{+1.7}_{-1.6}$ |
| $\gamma_{MINERVA-3}$ (m s$^{-1}$) | $N(0, 50)$ | $-54.5^{+3.4}_{-3.1}$ |
| $\gamma_{MINERVA-4}$ (m s$^{-1}$) | $N(0, 50)$ | $27.1^{+2.6}_{-2.5}$ |
| $\gamma_{NRES}$ (m s$^{-1}$) | $N(0, 50)$ | $-0.7^{+6.7}_{-6.8}$ |
| $\sigma_{CHIRON}$ (m s$^{-1}$) | $LU(0.01, 50)$ | $0.018^{+0.02}_{-0.006}$ |
| $\sigma_{FEROS}$ (m s$^{-1}$) | $LU(0.01, 50)$ | $4.1^{+1.7}_{-1.3}$ |
| $\sigma_{MINERVA-3}$ (m s$^{-1}$) | $LU(0.01, 50)$ | $14.7^{+3.5}_{-2.5}$ |
| $\sigma_{MINERVA-4}$ (m s$^{-1}$) | $LU(0.01, 50)$ | $22.4^{+2.3}_{-1.9}$ |
| $\sigma_{NRES}$ (ms$^{-1}$) | $LU(0.01, 50)$ | $33^{+10}_{-10}$ |
| $\sigma^{GP}_{TESS-3}$ | $LU(10^{-5}, 10^2)$ | $0.00031^{+0.00003}_{-0.00003}$ |
| $\sigma^{GP}_{TESS-6}$ | $LU(10^{-5}, 10^2)$ | $0.00021^{+0.00004}_{-0.00003}$ |
| $\sigma^{GP}_{TESS-7}$ | $LU(10^{-5}, 10^2)$ | $0.00014^{+0.00003}_{-0.00002}$ |
| $\sigma^{GP}_{TESS-9}$ | $LU(10^{-5}, 10^2)$ | $0.00018^{+0.00002}_{-0.00002}$ |
| $\sigma^{GP}_{TESS-10}$ | $LU(10^{-5}, 10^2)$ | $0.00017^{+0.00002}_{-0.00002}$ |
| $\sigma^{GP}_{TESS-13}$ | $LU(10^{-5}, 10^2)$ | $0.003^{+0.005}_{-0.002}$ |
| $\rho^{GP}_{TESS-3}$ | $LU(10^{-2}, 10^2)$ | $0.37^{+0.07}_{-0.05}$ |
| $\rho^{GP}_{TESS-6}$ | $LU(10^{-2}, 10^2)$ | $0.95^{+0.21}_{-0.16}$ |
| $\rho^{GP}_{TESS-7}$ | $LU(10^{-2}, 10^2)$ | $0.9^{+0.3}_{-0.2}$ |
| $\rho^{GP}_{TESS-9}$ | $LU(10^{-2}, 10^2)$ | $0.35^{+0.05}_{-0.05}$ |
| $\rho^{GP}_{TESS-10}$ | $LU(10^{-2}, 10^2)$ | $0.47^{+0.07}_{-0.06}$ |
| $\rho^{GP}_{TESS-13}$ | $LU(10^{-2}, 10^2)$ | $21^{+23}_{-11}$ |
| $b$ | | $0.15^{+0.05}_{-0.05}$ |
| $R_P/R_\star$ | | $0.0614^{+0.0002}_{-0.0002}$ |
| $e$ | | $0.153^{+0.006}_{-0.007}$ |
| $\omega$ (deg) | | $64.8^{+1.8}_{-1.8}$ |
| $i$ (deg) | | $89.2^{+0.3}_{-0.3}$ |
| $M_P$ ($M_J$) | | $1.53^{+0.03}_{-0.03}$ |
| $R_P$ ($R_J$) | | $0.99^{+0.01}_{-0.01}$ |
| $a$ (au) | | $0.097^{+0.001}_{-0.001}$ |
| $T_{eq}$ (K)[b] | | $1370^{+10}_{-10}$ |

**Notes.** For the priors, $N(\mu, \sigma)$ stands for a normal distribution with mean $\mu$ and standard deviation $\sigma$, $U(a, b)$ stands for a uniform distribution between $a$ and $b$, and $LU(a, b)$ stands for a log-uniform prior defined between $a$ and $b$.

[a] These parameters correspond to the parameterization presented in Espinoza (2019b) for sampling physically possible combinations of $b$ and $R_P/R_\star$.

[b] Time-averaged equilibrium temperature computed according to Equation (16) of Méndez & Rivera-Valentín (2017).

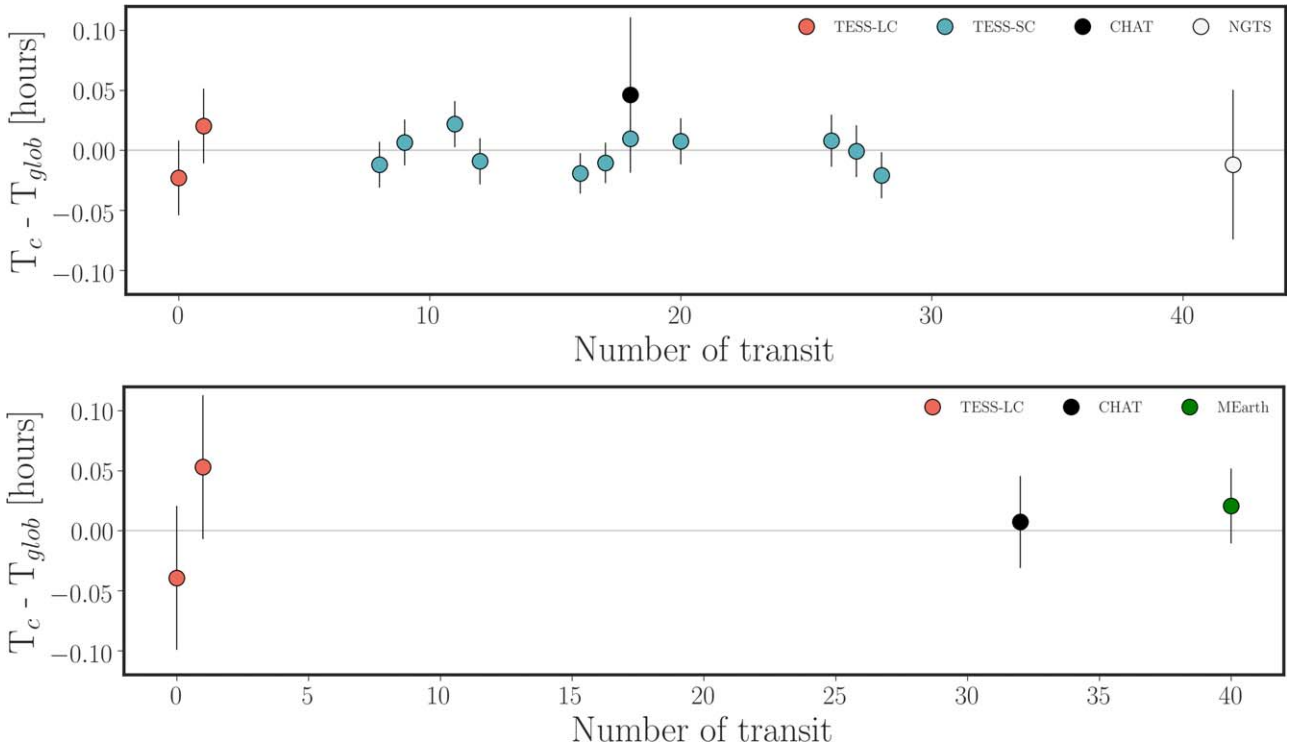


**Figure 9.** Transit timing variations for TOI-481 b (top panel) and TOI-892 b (bottom panel) computed from the TESS and ground-based light curves. No significant signal is identified in both cases.

**Table 5**
Same as Table 5, But for TOI-892 b. $J(a, b)$ Stands for a Jeffrey's Prior Defined between $a$ and $b$

| Parameter | Prior | Value |
|---|---|---|
| $P$ (days) | $N(10.6, 1.0)$ | $10.62656^{+0.00007}_{-0.00007}$ |
| $T_0$ (BJD) | $N(2458475.7, 1.0)$ | $2458475.689^{+0.002}_{-0.002}$ |
| $a/R_\star$ | $U(1, 300)$ | $14.2^{+0.8}_{-0.7}$ |
| $R_P/R_\star$ | $U(0.0001, 1)$ | $0.079^{+0.001}_{-0.001}$ |
| $b$ | $U(0, 1)$ | $0.43^{+0.09}_{-0.13}$ |
| $K$ (km s$^{-1}$) | $U(0, 1)$ | $0.074^{+0.005}_{-0.005}$ |
| $q_1^{\rm TESS}$ | $U(0, 1)$ | $0.4^{+0.2}_{-0.2}$ |
| $q_2^{\rm TESS}$ | $U(0, 1)$ | $0.4^{+0.3}_{-0.3}$ |
| $q_1^{\rm CHAT}$ | $U(0, 1)$ | $0.6^{+0.2}_{-0.2}$ |
| $q_1^{\rm MEarth}$ | $U(0, 1)$ | $0.90^{+0.08}_{-0.13}$ |
| $\sigma_w^{\rm TESS}$ (ppm) | $J(10^0, 10^3)$ | $553^{+20}_{-21}$ |
| $\sigma_w^{\rm CHAT}$ (ppm) | $J(10^0, 10^3)$ | $1046^{+69}_{-70}$ |
| $\sigma_w^{\rm MEarth}$ (ppm) | $J(10^0, 10^3)$ | $869^{+77}_{-77}$ |
| $\gamma_{\rm FEROS}$ (km s$^{-1}$) | $N(42.02, 0.010)$ | $42.033^{+0.005}_{-0.005}$ |
| $\gamma_{\rm TRES}$ (km s$^{-1}$) | $N(0.04.0, 0.010)$ | $0.05^{+0.01}_{-0.01}$ |
| $\sigma_{\rm FEROS}$ (km s$^{-1}$) | $N(0.001, 0.1)$ | $0.012^{+0.006}_{-0.006}$ |
| $\sigma_{\rm TRES}$ (km s$^{-1}$) | $N(0.001, 0.1)$ | $0.005^{+0.010}_{-0.003}$ |
| $\sigma_{\rm TESS}^{GP}$ | $J(10^{-5}, 10^3)$ | $363^{+70}_{-51}$ |
| $\rho_{\rm TESS}^{GP}$ | $J(10^{-5}, 10^3)$ | $0.6^{+0.2}_{-0.2}$ |
| $e$ | | <0.125 (98% confidence) |
| $i$ (deg) | | $88.2^{+0.3}_{-0.5}$ |
| $\rho_\star$ (kg m$^{-3}$) | | $482^{+82}_{-72}$ |
| $M_P$ ($M_J$) | | $0.95^{+0.07}_{-0.07}$ |
| $R_P$ ($R_J$) | | $1.07^{+0.02}_{-0.02}$ |
| $a$ (au) | | $0.092^{+0.005}_{-0.005}$ |
| $T_{\rm eq}$ (K) | | $1397^{+40}_{-40}$ |

spectrograph. We found that the joint modeling with zero eccentricity delivers a higher log evidence than the eccentric version, and we adopted the posterior parameters of that model, which are presented in Table 5 along with the derived planet parameters.

By combining the posterior parameters of the adopted joint fit with the stellar properties of TOI-892 we find that TOI-892 b has a mass of $M_P = 0.95^{+0.07}_{-0.07}$ $M_J$, a radius of $R_P = 1.07^{+0.02}_{-0.02}$ $R_J$, and an equilibrium temperature of $T_{\rm eq} = 1397^{+40}_{-40}$ K. We determine a 98% upper limit for the orbital eccentricity of TOI-892 b of 0.125.

### 3.4. Timing of Transits and Additional Photometric Signals

We searched for variations in the time of transits of TOI-481 b and TOI-892 b that could originate from gravitational interactions with other planets in each system. For this procedure we performed independent `juliet` runs for each one of the transits of the TESS and follow-up light curves. We fix most of the parameters to those obtained in the global analysis, but allowed the time of transit and the transit depth to vary. The transit timing variations for TOI-481 b and TOI-892 b are displayed in Figure 9. No significant variations in the timing of transits are identified for both systems.

We also searched for additional transiting candidates in the TESS data of both systems by masking out the transits of TOI-481 b and TOI-892 b, and running the box least-squares (Kovács et al. 2002) algorithm. No significant signals were identified.

## 4. Discussion

TOI-481 b and TOI-892 b are both compared in Figure 10 with the population of well-characterized transiting giant planets

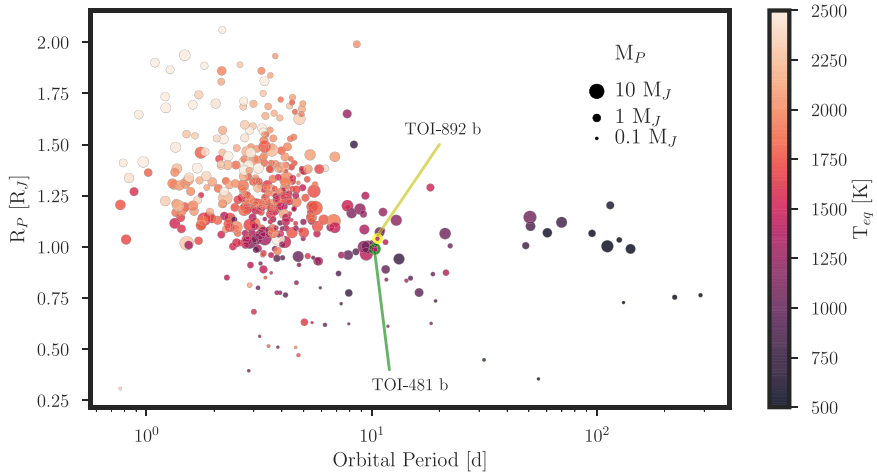


**Figure 10.** Mass–period diagram for the population of transiting giant planets ($M_P > 0.1\ M_J$) having masses and radii measured with a precision of 20% or better. The points are color coded by equilibrium temperature and the pint size scales with the planet mass.

($M_P > 0.1\ M_J$) in the planetary radius versus orbital period space. Both planets join the population of moderately long-period ($P > 10$ days) giant planets, which has just recently started to see an increase in the number of detected systems. In terms of physical and orbital properties TOI-481 b is similar to WASP-134 b ($M_P = 1.41 \pm 0.08\ M_J$, $R_P = 0.99 \pm 0.06\ R_J$, $P = 10.2$ days; Anderson et al. 2018). On the other hand, TOI-892 b shares similar properties with WASP-185 b (Hellier et al. 2019), which has a mass of $M_P = 0.98 \pm 0.06\ M_J$, a radius of $R_P = 1.25 \pm 0.08\ R_J$, and an orbital period of $P = 9.4$ days, but as opposed to TOI-892 b has a significantly eccentric orbit ($e = 0.23 \pm 0.04$).

Despite having periods longer than 10 days, both TOI-481 b and TOI-892 b have moderately high equilibrium temperatures, due to the high luminosity of their host stars. Their equilibrium temperatures are somewhat higher than 1000 K, and therefore these planets are just in the region where the inflation mechanism of hot Jupiters starts to have an impact on the structure of the planet (Demory & Seager 2011; Laughlin et al. 2011). The measured radius for TOI-892 b is in good agreement with the mean radius of other hot Jupiters having similar insolation levels, which is of $1.1 \pm 0.1\ R_J$ for $1300 < T_{eq} < 1500$. The radius of TOI-481 b, while still consistent with this distribution, is significantly more compact than that of TOI-892 b. In this context it is important to note that TOI-481 is in the final stages of the main-sequence evolution and has started to receive increased levels of irradiation during the last gigayear of evolution. Its non-inflated radius can be linked with a shallow level deposition of the stellar energy into the planet interior during main-sequence evolution as argued by Komacek et al. (2020), which is not enough to re-inflate the planet even at temperatures higher than 1000 K. If warm Jupiters are efficiently re-inflated during post-main-sequence evolution, as some recent studies have proposed (Grunblatt et al. 2016, 2017; Jones et al. 2018), then some other mechanism should operate to allow the deposition of energy deeper in the planet interior.

Both systems are well-suited objects to perform Rossiter–McLaughlin observations (McLaughlin 1924; Rossiter 1924) for measuring their stellar obliquities (e.g., Triaud et al. 2010). Given the properties of each system, we expect them to have Rossiter–McLaughlin signals with semi-amplitudes of 15 m s$^{-1}$ and 47 m s$^{-1}$, for TOI-481 b and TOI-892 b, respectively, for aligned orbits, which can be measured with typical facilities having a stabilized high-resolution echelle spectrograph. Spin–orbit angles of giant planets with orbital separations larger than $\gtrsim$0.1 au are expected to be particularly useful for constraining migration scenarios, because at these moderately long orbital distances, tidal interactions are not supposed to be strong enough for realigning the rotation of the outer layers of the star with the orbital plane (Albrecht et al. 2012; Dawson 2014). The low eccentricities of the orbits of TOI-481 b and TOI-892 b and the absence of close planet companions, based on the radial velocity and photometric data, points to interactions with the protoplanetary disk as the most probable migration scenario for these systems (Dong et al. 2014).

We acknowledge the use of public TESS Alert data from pipelines at the TESS Science Office and at the TESS Science Processing Operations Center. This research has made use of the exoplanet follow-up observation program website, which is operated by the California Institute of Technology, under contract with the National Aeronautics and Space Administration under the Exoplanet Exploration Program. This paper includes data collected by the TESS mission, which are publicly available from the Mikulski Archive for Space Telescopes (MAST). Resources supporting this work were provided by the NASA High-End Computing (HEC) Program through the NASA Advanced Supercomputing (NAS) Division at Ames Research Center for the production of the SPOC data products. R.B. acknowledges support from FONDECYT Postdoctoral Fellowship Project 3180246, and from ANID - Millennium Science Initiative—ICN12_009. A.J. acknowledges support from FONDECYT project 1171208, and from ANID—Millennium Science Initiative—ICN12_009.

J.I.V. acknowledges support of CONICYT-PFCHA/Doctorado Nacional-21191829. This work was supported by the DFG Research Unit FOR2544 "Blue Planets around Red Stars," project no. RE 2694/4-1. We thank Paul Eigenthaler, Angela Hempel, Maren Hempel, Sam Kim, and Régis Lachaume for their technical assistance during the observations at the MPG 2.2 m Telescope. We thank the Swiss National Science Foundation (SNSF) and the Geneva University for their continuous support to our planet search programs. This work has been in particular carried out in the frame of the National Centre for Competence in Research PlanetS supported by the Swiss National Science Foundation (SNSF). MINERVA-

Australis is supported by Australian Research Council LIEF Grant LE160100001, Discovery Grant DP180100972, Mount Cuba Astronomical Foundation, and institutional partners University of Southern Queensland, UNSW Sydney, MIT, Nanjing University, George Mason University, University of Louisville, University of California Riverside, University of Florida, and The University of Texas at Austin. This research was supported by grant No. 2016069 of the United States-Israel Binational Science Foundation (BSF) The MEarth Team gratefully acknowledges funding from the David and Lucile Packard Fellowship for Science and Engineering (awarded to D.C.). This material is based upon work supported by the National Science Foundation under grants AST-0807690, AST-1109468, AST-1004488 (Alan T. Waterman Award), and AST- 1616624, and upon work supported by the National Aeronautics and Space Administration under grant No. 80NSSC18K0476 issued through the XRP Program. This work is made possible by a grant from the John Templeton Foundation. The opinions expressed in this publication are those of the authors and do not necessarily reflect the views of the John Templeton Foundation. We respectfully acknowledge the traditional custodians of all lands throughout Australia, and recognize their continued cultural and spiritual connection to the land, waterways, cosmos, and community. We pay our deepest respects to all Elders, ancestors, and descendants of the Giabal, Jarowair, and Kambuwal nations, upon whose lands the MINERVA-Australis facility at Mt. Kent is situated.

R.B. acknowledges support from CORFO project N° 14ENI2-26865.

*Facilities: Astrometry*: Gaia (Gaia Collaboration et al. 2016, 2018). *Imaging*: SOAR (HRCam; Tokovinin 2018). *Spectroscopy*: CTIO1.5m (CHIRON; Tokovinin et al. 2013), MPG2.2m (FEROS; Kaufer et al. 1999), Euler1.2m (CORALIE; Mayor et al. 2003), Tillinghast1.5m (TRES) (Fűrész 2008), MINERVA-Australis (Addison et al. 2019), NRES (Siverd et al. 2018), *Photometry*: CHAT:0.7m, MEarth-South (Irwin et al. 2015), NGTS (Wheatley et al. 2018), TESS (Ricker et al. 2015).

*Software:* `juliet` (Espinoza et al. 2019b), `CERES` (Jordán et al. 2014; Brahm et al. 2017a), `ZASPE` (Brahm et al. 2015, 2017b), `radvel` (Fulton et al. 2018) `emcee` (Foreman-Mackey et al. 2013), MultiNest (Feroz et al. 2009), `batman` (Kreidberg et al. 2015), `SPC` (Buchhave et al. 2012), `SpecMatch` (Yee et al. 2017).

## ORCID iDs

Rafael Brahm https://orcid.org/0000-0002-9158-7315
Louise D. Nielsen https://orcid.org/0000-0002-5254-2499
Robert A. Wittenmyer https://orcid.org/0000-0001-9957-9304
Songhu Wang https://orcid.org/0000-0002-7846-6981
Joseph E. Rodriguez https://orcid.org/0000-0001-8812-0565
Néstor Espinoza https://orcid.org/0000-0001-9513-1449
Andrés Jordán https://orcid.org/0000-0002-5389-3944
Melissa Hobson https://orcid.org/0000-0002-5945-7975
Diana Kossakowski https://orcid.org/0000-0002-0436-7833
Paula Sarkis https://orcid.org/0000-0001-8128-3126
Martin Schlecker https://orcid.org/0000-0001-8355-2107
Trifon Trifonov https://orcid.org/0000-0002-0236-775X
Sahar Shahaf https://orcid.org/0000-0001-9298-8068
George Ricker https://orcid.org/0000-0003-2058-6662
Roland Vanderspek https://orcid.org/0000-0001-6763-6562
David W. Latham https://orcid.org/0000-0001-9911-7388
Sara Seager https://orcid.org/0000-0002-6892-6948
Joshua N. Winn https://orcid.org/0000-0002-4265-047X
Jon M. Jenkins https://orcid.org/0000-0002-4715-9460
Brett C. Addison https://orcid.org/0000-0003-3216-0626
Gáspár Á. Bakos https://orcid.org/0000-0001-7204-6727
Waqas Bhatti https://orcid.org/0000-0002-0628-0088
Daniel Bayliss https://orcid.org/0000-0001-6023-1335
Allyson Bieryla https://orcid.org/0000-0001-6637-5401
Brendan P. Bowler https://orcid.org/0000-0003-2649-2288
Timothy M. Brown https://orcid.org/0000-0001-5062-0847
Douglas A. Caldwell https://orcid.org/0000-0003-1963-9616
David Charbonneau https://orcid.org/0000-0002-9003-484X
Karen A. Collins https://orcid.org/0000-0001-6588-9574
Allen B. Davis https://orcid.org/0000-0002-5070-8395
Gilbert A. Esquerdo https://orcid.org/0000-0002-9789-5474
Benjamin J. Fulton https://orcid.org/0000-0003-3504-5316
Natalia M. Guerrero https://orcid.org/0000-0002-5169-9427
Aleisha Hogan https://orcid.org/0000-0001-9658-1767
Jonathan Horner https://orcid.org/0000-0002-1160-7970
Chelsea X. Huang https://orcid.org/0000-0003-0918-7484
Stephen R. Kane https://orcid.org/0000-0002-7084-0529
John Kielkopf https://orcid.org/0000-0003-0497-2651
Andrew W. Mann https://orcid.org/0000-0003-3654-1602
James McCormac https://orcid.org/0000-0003-1631-4170
Curtis McCully https://orcid.org/0000-0001-5807-7893
Ismael Mireles https://orcid.org/0000-0002-4510-2268
Jack Okumura https://orcid.org/0000-0002-4876-8540
Peter Plavchan https://orcid.org/0000-0002-8864-1667
Samuel N. Quinn https://orcid.org/0000-0002-8964-8377
Markus Rabus https://orcid.org/0000-0003-2935-7196
Joshua E. Schlieder https://orcid.org/0000-0001-5347-7062
Avi Shporer https://orcid.org/0000-0002-1836-3120
Robert J. Siverd https://orcid.org/0000-0001-5016-3359
Keivan G. Stassun https://orcid.org/0000-0002-3481-9052
Vincent Suc https://orcid.org/0000-0001-7070-3842
Thiam-Guan Tan https://orcid.org/0000-0001-5603-6895
Chris G. Tinney https://orcid.org/0000-0002-7595-0970
Stephane Udry https://orcid.org/0000-0001-7576-6236
Jose I. Vines https://orcid.org/0000-0002-1896-2377
Maja Vuckovic https://orcid.org/0000-0001-8339-6423
Duncan J. Wright https://orcid.org/0000-0001-7294-5386
Daniel A. Yahalomi https://orcid.org/0000-0003-4755-584X
Abner Zapata https://orcid.org/0000-0003-2326-6488
Hui Zhang https://orcid.org/0000-0003-3491-6394
Carl Ziegler https://orcid.org/0000-0002-0619-7639

## References

Addison, B., Wright, D. J., Wittenmyer, R. A., et al. 2019, PASP, 131, 115003
Addison, B. C., Wright, D. J., Nicholson, B. A., et al. 2020, arXiv:2001.07345
Albrecht, S., Winn, J. N., Johnson, J. A., et al. 2012, ApJ, 757, 18
Almenara, J. M., Díaz, R. F., Hébrard, G., et al. 2018, A&A, 615, A90
Anderson, D. R., Bouchy, F., Brown, D. J. A., et al. 2018, arXiv:1812.09264
Auvergne, M., Bodin, P., Boisnard, L., et al. 2009, A&A, 506, 411
Bakos, G., Noyes, R. W., Kovács, G., et al. 2004, PASP, 116, 266
Barclay, T., Pepper, J., & Quintana, E. V. 2018, ApJS, 239, 2
Barnes, S. I., Gibson, S., Nield, K., & Cochrane, D. 2012, Proc. SPIE, 8446, 844688
Batygin, K., & Brown, M. E. 2010, ApJ, 716, 1323
Beaugé, C., & Nesvorný, D. 2012, ApJ, 751, 119
Bodenheimer, P., Lin, D. N. C., & Mardling, R. A. 2001, ApJ, 548, 466
Bonomo, A. S., Santerne, A., Alonso, R., et al. 2010, A&A, 520, A65
Borucki, W. J., Koch, D., Basri, G., et al. 2010, Sci, 327, 977
Brahm, R., Espinoza, N., Jordán, A., et al. 2018, MNRAS, 477, 2572
Brahm, R., Espinoza, N., Jordán, A., et al. 2019, AJ, 158, 45
Brahm, R., Jordán, A., & Espinoza, N. 2017a, PASP, 129, 034002
Brahm, R., Jordán, A., Hartman, J., & Bakos, G. 2017b, MNRAS, 467, 971

Brahm, R., Jordán, A., Hartman, J. D., et al. 2015, AJ, 150, 33
Bressan, A., Marigo, P., Girardi, L., et al. 2012, MNRAS, 427, 127
Brown, T. M., Baliber, N., Bianco, F. B., et al. 2013, PASP, 125, 1031
Bryant, E. M., Bayliss, D., McCormac, J., et al. 2020, MNRAS, 494, 5872
Buchhave, L. A., Bakos, G. Á, Hartman, J. D., et al. 2010, ApJ, 720, 1118
Buchhave, L. A., Latham, D. W., Johansen, A., et al. 2012, Natur, 486, 375
Buchner, J., Georgakakis, A., Nandra, K., et al. 2014, A&A, 564, A125
Castelli, F., & Kurucz, R. L. 2003, in IAU Symp. 210, Modeling of Stellar Atmospheres, ed. N. Piskunov, W. W. Weiss, & D. F. Gray (San Fransisco, CA: ASP), A20
Charbonneau, D., Brown, T. M., Noyes, R. W., & Gilliland, R. L. 2002, ApJ, 568, 377
Cooke, B. F., Pollacco, D., & Bayliss, D. 2019, A&A, 631, A83
Bakos, G. Á, Csubry, Z., Penev, K., et al. 2013, PASP, 125, 154
Dawson, R. I. 2014, ApJL, 790, L31
Dawson, R. I., & Johnson, J. A. 2018, ARA&A, 56, 175
Deeg, H. J., Moutou, C., Erikson, A., et al. 2010, Natur, 464, 384
Demory, B.-O., & Seager, S. 2011, ApJS, 197, 12
Dong, S., Katz, B., & Socrates, A. 2014, ApJL, 781, L5
Engel, M., Shahaf, S., & Mazeh, T. 2017, PASP, 129, 065002
Espinoza, N. 2018, RNAAS, 2, 209
Espinoza, N., Hartman, J. D., Bakos, G. Á, et al. 2019a, AJ, 158, 63
Espinoza, N., Kossakowski, D., & Brahm, R. 2019b, MNRAS, 490, 2262
Feroz, F., Hobson, M. P., & Bridges, M. 2009, MNRAS, 398, 1601
Fűrész, G. 2008, PhD thesis, University of Szeged, Hungary
Foreman-Mackey, D., Agol, E., Angus, R., & Ambikasaran, S. 2017, AJ, 154, 220
Foreman-Mackey, D., Hogg, D. W., Lang, D., & Goodman, J. 2013, PASP, 125, 306
Fulton, B. J., Petigura, E. A., Blunt, S., & Sinukoff, E. 2018, PASP, 130, 044504
Gaia Collaboration, Brown, A. G. A., Vallenari, A., et al. 2016, A&A, 595, A2
Gaia Collaboration, Brown, A. G. A., Vallenari, A., et al. 2018, A&A, 616, A1
Gaudi, B. S., Seager, S., & Mallen-Ornelas, G. 2005, ApJ, 623, 472
Gill, S., Wheatley, P. J., Cooke, B. F., et al. 2020, ApJL, 898, L11
Grunblatt, S. K., Huber, D., Gaidos, E., et al. 2017, AJ, 154, 254
Grunblatt, S. K., Huber, D., Gaidos, E. J., et al. 2016, AJ, 152, 185
Hébrard, G., Ehrenreich, D., Bouchy, F., et al. 2011, A&A, 527, L11
Hellier, C., Anderson, D. R., Barkaoui, K., et al. 2019, MNRAS, 490, 1479
Howell, S. B., Sobeck, C., Haas, M., et al. 2014, PASP, 126, 398
Huang, X., Burt, J., Vanderburg, A., et al. 2019, AAS Meeting, 233, 209.08
Huber, D., Chaplin, W. J., Chontos, A., et al. 2019, AJ, 157, 245
Husser, T. O., Wende-von Berg, S., Dreizler, S., et al. 2013, A&A, 553, A6
Irwin, J. M., Berta-Thompson, Z. K., Charbonneau, D., et al. 2015, in 18th Cambridge Workshop on Cool Stars, Stellar Systems, and the Sun, ed. G. van Belle & H. C. Harris (San Fransisco, CA: ASP), 767
Jenkins, J. M., Twicken, J. D., McCauliff, S., et al. 2016, Proc. SPIE, 9913, 99133E
Jones, M. I., Brahm, R., Espinoza, N., et al. 2018, A&A, 613, A76
Jones, M. I., Brahm, R., Espinoza, N., et al. 2019, A&A, 625, A16
Jordán, A., Brahm, R., Bakos, G. Á, et al. 2014, AJ, 148, 29
Jordán, A., Brahm, R., Espinoza, N., et al. 2019, AJ, 157, 100
Jordán, A., Brahm, R., Espinoza, N., et al. 2020, AJ, 159, 145
Kaufer, A., Stahl, O., Tubbesing, S., et al. 1999, Msngr, 95, 8
Kipping, D. M. 2013, MNRAS, 435, 2152
Komacek, T. D., Thorngren, D. P., Lopez, E. D., & Ginzburg, S. 2020, ApJ, 893, 36
Kovács, G., Zucker, S., & Mazeh, T. 2002, A&A, 391, 369
Kreidberg, L., Line, M. R., Bean, J. L., et al. 2015, ApJ, 814, 66
Kurokawa, H., & Inutsuka, S.-i. 2015, ApJ, 815, 78
Laughlin, G., Crismani, M., & Adams, F. C. 2011, ApJL, 729, L7
Leconte, J., Chabrier, G., Baraffe, I., & Levrard, B. 2010, A&A, 516, A64
Li, J., Tenenbaum, P., Twicken, J. D., et al. 2019, PASP, 131, 024506
Lopez, E. D., & Fortney, J. J. 2016, ApJ, 818, 4
Mayor, M., Pepe, F., Queloz, D., et al. 2003, Msngr, 114, 20
Mayor, M., & Queloz, D. 1995, Natur, 378, 355
McLaughlin, D. B. 1924, ApJ, 60, 22
Méndez, A., & Rivera-Valentín, E. G. 2017, ApJL, 837, L1
Munari, U., Henden, A., Frigo, A., et al. 2014, AJ, 148, 81
Naoz, S., Farr, W. M., & Rasio, F. A. 2012, ApJL, 754, L36
Nielsen, L. D., Bouchy, F., Turner, O., et al. 2019, A&A, 623, A100
Pepper, J., Pogge, R. W., DePoy, D. L., et al. 2007, PASP, 119, 923
Pollacco, D. L., Skillen, I., Collier Cameron, A., et al. 2006, PASP, 118, 1407
Pont, F., Knutson, H., Gilliland, R. L., Moutou, C., & Charbonneau, D. 2008, MNRAS, 385, 109
Queloz, D., Anderson, D. R., Collier Cameron, A., et al. 2010, A&A, 517, L1
Ricker, G. R., Winn, J. N., Vanderspek, R., et al. 2015, JATIS, 1, 014003
Rodriguez, J. E., Quinn, S. N., Huang, C. X., et al. 2019, AJ, 157, 191
Rossiter, R. A. 1924, ApJ, 60, 15
Shporer, A., Zhou, G., Fulton, B. J., et al. 2017, AJ, 154, 188
Siverd, R. J., Brown, T. M., Barnes, S., et al. 2018, Proc. SPIE, 10702, 107026C
Skrutskie, M. F., Cutri, R. M., Stiening, R., et al. 2006, AJ, 131, 1163
Smith, J. C., Stumpe, M. C., Van Cleve, J. E., et al. 2012, PASP, 124, 1000
Southworth, J. 2011, MNRAS, 417, 2166
Speagle, J. S. 2020, MNRAS, 493, 3132
Stassun, K. G., Corsaro, E., Pepper, J. A., & Gaudi, B. S. 2018a, AJ, 155, 22
Stassun, K. G., Oelkers, R. J., Pepper, J., et al. 2018b, AJ, 156, 102
Stumpe, M. C., Smith, J. C., Catanzarite, J. H., et al. 2014, PASP, 126, 100
Stumpe, M. C., Smith, J. C., Van Cleve, J. E., et al. 2012, PASP, 124, 985
Sullivan, P. W., Winn, J. N., Berta-Thompson, Z. K., et al. 2015, ApJ, 809, 77
Thorngren, D. P., Fortney, J. J., Murray-Clay, R. A., & Lopez, E. D. 2016, ApJ, 831, 64
Tokovinin, A. 2018, PASP, 130, 035002
Tokovinin, A., Fischer, D. A., Bonati, M., et al. 2013, PASP, 125, 1336
Triaud, A. H. M. J., Collier Cameron, A., Queloz, D., et al. 2010, A&A, 524, A25
Twicken, J. D., Catanzarite, J. H., Clarke, B. D., et al. 2018, PASP, 130, 064502
Vidal-Madjar, A., Lecavelier des Etangs, A., Désert, J. M., et al. 2003, Natur, 422, 143
Wang, J., Fischer, D. A., Horch, E. P., & Huang, X. 2015, ApJ, 799, 229
Wang, S., Jones, M., Shporer, A., et al. 2019, AJ, 157, 51
Wheatley, P. J., West, R. G., Goad, M. R., et al. 2018, MNRAS, 475, 4476
Winn, J. N., Johnson, J. A., Howard, A. W., et al. 2010, ApJL, 723, L223
Wu, Y., & Lithwick, Y. 2011, ApJ, 735, 109
Yee, S. W., Petigura, E. A., & von Braun, K. 2017, ApJ, 836, 77
Zhou, G., Huang, C. X., Bakos, G. Á, et al. 2019, AJ, 158, 141
Ziegler, C., Tokovinin, A., Briceño, C., et al. 2020, AJ, 159, 19